Optimized thermodynamic properties of REE aqueous species (REE^{3+} and $REEOH^{2+}$) and experimental database for modeling the solubility of REE phosphate minerals (monazite, xenotime, and rhabdophane) from 25 to 300 °C

Ruiguang Pan [a,d,*], Alexander P. Gysi [a,b], George D. Miron [c], Chen Zhu [d]

[a] New Mexico Bureau of Geology and Mineral Resources, New Mexico Institute of Mining and Technology, Socorro, NM 87801, USA

[b] Department of Earth and Environmental Science, New Mexico Institute of Mining and Technology, Socorro, NM 87801, USA

[c] Paul Scherrer Institute, Laboratory for Waste Management, Villigen PSI 5232, Switzerland

[d] Department of Earth and Atmospheric Sciences, Indiana University, Bloomington, IN 47405, USA

*Corresponding author:

E-mail address: panr@iu.edu (R. Pan)

ORCID ID #: 0000-0003-2489-6545

Highlights:

- Thermodynamic properties of REE species (REE^{3+} and $REEOH^{2+}$) were optimized with available experimental solubility data for monazite, xenotime, and rhabdophane conducted in acidic fluids at 25–300 °C.
- The solubility of all monazite endmembers is controlled by both light REE^{3+} and $REEOH^{2+}$ species whereas xenotime solubility is controlled by the heavy REE^{3+} species at the studied conditions.
- The retrieved thermodynamic properties of REE aqueous species and experimental database are both available open access and build the framework for future extensions and optimizations.
- This study provides a comprehensive experimental database for REE implemented in the program GEMSFITS to conduct thermodynamic parameter optimizations.

Abstract

Rare earth elements (REE) are critical elements found in monazite, xenotime, and hydrated REE phosphates which typically form in hydrothermal mineral deposits. Accurate predictions of the solubility of these REE phosphates and the speciation of REE in aqueous fluids are both key to understanding the controls on the transport, fractionation, and deposition of REE in natural systems. Previous monazite and xenotime solubility experiments indicate the presence of large discrepancies between experimentally derived solubility constants versus calculated solubilities by combining different data sources for the thermodynamic properties of minerals and aqueous species at hydrothermal conditions. In this study, these discrepancies were resolved by using the program GEMSFITS to optimize the standard partial molal Gibbs energy of formation ($\Delta_f G^\circ_{298}$) of REE aqueous species (REE^{3+} and REE hydroxyl complexes) at 298.15 K and 1 bar while keeping the thermodynamic properties fixed for the REE phosphates. A comprehensive experimental database was compiled using solubility data available between 25 and 300 °C. The latter permits conducting thermodynamic parameter optimization of $\Delta_f G^\circ_{298}$ for REE aqueous species. Optimal matching of the rhabdophane solubility data between 25 and 100 °C requires modifying the $\Delta_f G^\circ_{298}$ values of REE^{3+} by 1–6 kJ/mol, whereas matching of the monazite solubility data between 100 and 300 °C requires modifying the $\Delta_f G^\circ_{298}$ values of both REE^{3+} and $REEOH^{2+}$ by ~15–31 kJ/mol and ~2–10 kJ/mol, respectively. For xenotime, adjustments of $\Delta_f G^\circ_{298}$ values by 1–26 kJ/mol are only necessary for the REE^{3+} species. The optimizations indicate that the solubility of monazite in acidic solutions is controlled by the light (L)REE^{3+} species at <150 °C and the $LREEOH^{2+}$ species at >150 °C, whereas the solubility of xenotime is controlled by the heavy (H)REE^{3+} species between 25 and 300 °C. Based on the optimization results, we conclude that the revised Helgeson-Kirkham-Flowers equation of state does not reliably predict the thermodynamic properties of REE^{3+}, $REEOH^{2+}$, and likely other REE hydroxyl species at hydrothermal conditions. We therefore provide an experimental database (ThermoExp_REE) as a basic framework for future updates, extensions with other ligands, and optimizations as new experimental REE data become available. The optimized thermodynamic properties of aqueous species and minerals are available open access to accurately predict the solubility of REE phosphates in fluid-rock systems.

Keywords: Thermodynamic database; Hydrothermal fluids; Geochemical modeling; Monazite; Xenotime; Rhabdophane

1. Introduction

It has long been recognized that aqueous fluids can play an important role in the mobilization of rare earth elements (REE) in natural hydrothermal systems (Bau and Dulski, 1999; Lottermoser, 1992; Michard, 1989), and even control the final stages of formation of REE mineral deposits (Gysi et al., 2016; Verplanck, 2017; Verplanck et al., 2022; Williams-Jones et al., 2000). The solubility of REE phosphates, including monazite and xenotime, commonly constrains the mobility of REE in natural hydrothermal fluids. This includes, for example, the replacement of apatite by monazite/xenotime in the Pea Ridge iron-oxide-apatite REE deposit in Missouri (Harlov et al., 2016), the presence of monazite-bearing veins from the giant Bayan Obo REE deposit in China (Smith et al., 1999, 2016), and the formation of sediment-hosted hydrothermal xenotime veins in the Browns Range in Australia (Cook et al., 2013; Richter et al., 2018). At low temperatures (<90 °C), the formation of the hydrated REE phosphates rhabdophane ($REEPO_4 \cdot nH_2O$) controls the mobility of REE, for example, during weathering of carbonatites (Andersen et al., 2017; Huang et al., 2021). Fluid-rock reaction path simulations permit predicting the REE mobilization, fractionation, and deposition mechanisms in these natural systems (Gysi and Williams-Jones, 2013; Migdisov et al., 2016; Migdisov and Williams-Jones, 2014; Perry and Gysi, 2018). However, the outcomes and accuracy of these simulations are strongly dependent on the underlying thermodynamic properties of aqueous species and minerals as a function of temperature and pressure.

To date, the formation constants of key REE aqueous complexes have been determined experimentally in acidic fluids up to 300–350 °C including for the fluoride, sulfate, and chloride complexes (Migdisov et al., 2009, 2016). Recent experimental studies have also identified the importance of REE hydroxyl and carbonate complexes in near-neutral to alkaline fluids (Louvel et al., 2022; Nisbet et al., 2022). The formation constants (i.e., logβ1, logβ2, etc.) determined experimentally permit deriving the thermodynamic properties of REE aqueous complexes, but nonetheless, these depend on the properties of the REE^{3+} ions (e.g., $REE^{3+} + Cl^- = REECl^{2+}$). The latter are commonly taken from tables presented by Sverjensky et al. (1997), which allow predicting the thermodynamic properties of aqueous species at elevated temperatures and pressures based on the revised Helgeson-Kirkham-Flowers (HKF) semi-empirical equation of state (Helgeson et al., 1981; Shock et al., 1992; Shock and Helgeson, 1988; Tanger and Helgeson, 1988). The thermodynamic database slop98.dat implemented in the program SUPCRT92 (Johnson et al., 1992) includes the latest updates from this work several decades ago (Haas et al., 1995; Shock et al., 1997; Sverjensky et al., 1997). This program has been more recently updated by Zimmer et al.

(2016). The tables for REE aqueous species and the HKF parameters estimated by Haas et al. (1995) are still the only comprehensive and internally consistent (but not necessarily accurate) thermodynamic data for REE aqueous species. The stability for many of these species (i.e., carbonate, phosphate, and hydroxyl complexes) has not yet been verified by measurements at elevated temperatures. Some of the predicted thermodynamic properties, such as the REE chloride and fluoride species, significantly deviate from the experimental measurements (Migdisov et al., 2009, 2016).

In contrast to the properties of REE aqueous species, the standard thermodynamic properties of REE phosphates have been intensively investigated. The thermodynamic properties of all light (L)REE monoclinic monazite endmembers ($LREEPO_4$; LREE: La to Gd) and heavy (H)REE tetragonal xenotime endmembers ($HREEPO_4$; Tb to Lu, plus Y) were determined from calorimetry (Gavrichev et al., 2008, 2010, 2012, 2013b, 2016; Popa et al., 2006b, 2007; Popa and Konings, 2006; Tyurin et al., 2020; Ushakov et al., 2001) and complemented by solubility experiments in hydrochloric and perchloric acid-based solutions between 100–300 °C (Cetiner et al., 2005; Gysi et al., 2015, 2018; Gysi and Harlov, 2021; Poitrasson et al., 2004; Van Hoozen et al., 2020). The thermodynamic properties of hydrated REE phosphates, including rhabdophane ($LREEPO_4 \cdot nH_2O$) and churchite ($HREEPO_4 \cdot nH_2O$), were determined by Shelyug et al. (2018) using calorimetry and their solubility products were determined by Gausse et al. (2016) between 25 and 90 °C. Other numerous comprehensive studies have determined the solubility products of hydrated REE phosphates at room temperature with a focus on seawater (Byrne and Kim, 1993; Firsching and Brune, 1991; Jonasson et al., 1985); this comprehensive work has recently been reviewed by Schijf and Byrne (2021). The structure of both anhydrous and hydrous REE phosphate endmembers was also determined in several studies (Boatner, 2002; Mesbah et al., 2017; Ni et al., 1995; Rafiuddin et al., 2014).

The thermodynamic properties of aqueous species and minerals are not always compatible with the experimentally determined solubility product. Recent experiments by Gysi et al. (2015, 2018) and Gysi and Harlov (2021) were conducted between 100 and 250 ºC under acidic conditions, and have shown that the solubility products of monazite and xenotime can differ by several orders of magnitude in comparison to the predicted values. The latter can be generated by combining the thermodynamic properties of REE aqueous species and existing HKF model parameters (Haas et al., 1995; Sverjensky et al., 1997) with the mineral properties determined from the calorimetric measurements. The discrepancies between experiments and predicted solubility constants were found to be most likely related to two major aqueous species including REE^{3+} and

132 $REEOH^{2+}$, which control the solubility of REE phosphates under acidic conditions (Gysi et al.,
133 2018; Gysi and Harlov, 2021). The thermodynamic properties of REE hydroxyl complexes are still
134 uncertain at elevated temperatures (Migdisov et al., 2016), and have only been determined for Nd
135 hydroxyl complexes above 100 °C (Wood et al., 2002). Nevertheless, thermodynamic optimization
136 approaches (Hingerl et al., 2014; Kinniburgh and Cooper, 2011; Miron et al., 2015) permit
137 reconciling the thermodynamic properties of aqueous species and minerals. The optimization of
138 Na, K, Ca, Mg, Si, and Al aqueous species was successfully conducted in the studies by Miron et
139 al. (2016, 2017) using the GEMSFITS (Miron et al., 2015) and GEMS (Kulik et al., 2013) code
140 packages. A similar approach was used by Gysi et al. (2018) and Gysi and Harlov (2021) to
141 evaluate the solubility of some of the monazite and xenotime endmembers.
142 In this study, experimental solubility data were compiled from 25 to 300 °C for monazite,
143 xenotime, and rhabdophane (Gausse et al., 2016; Gysi et al., 2015, 2018; Gysi and Harlov, 2021;
144 Van Hoozen et al., 2020) and the thermodynamic properties of REE aqueous species (REE^{3+} and
145 REE hydroxyl complexes) were optimized using GEMSFITS (Miron et al., 2015). This
146 comprehensive experimental database (ThermoExp_REE) and the optimized thermodynamic
147 properties for REE aqueous species allow to more accurately predict the solubility of REE
148 phosphates in hydrothermal fluids and highlight the need to revise the HKF parameters presented
149 by Haas et al. (1995). This work is part of an ongoing effort to improve the open access MINES
150 thermodynamic database (Gysi et al., 2023) maintained for simulating hydrothermal ore-forming
151 process and fluid-rock interaction (Gysi et al., 2015, 2018; Gysi and Harlov, 2021; Gysi and
152 Williams-Jones, 2013; Hurtig et al., 2018; Perry and Gysi, 2018).
153
154 **2. Thermodynamic framework**
155 *2.1. Speciation calculations and thermodynamic properties of minerals and aqueous species*
156 Experimental REE phosphate solubility data were compiled and evaluated in the REE-P-
157 O-H-Na-Cl system at temperatures between 25 and 300 °C at saturated water vapor pressure
158 (*swvp*). Speciation and chemical equilibrium between aqueous solutions and minerals were
159 calculated using the GEMS code package, which includes GEM-Selektor v.3
160 (http://gems.web.psi.ch/GEMS3) and the GEMS3K kernel (Kulik et al., 2013). Activity models
161 are implemented in GEMS through the built-in TSolMod library (Wagner et al., 2012). The
162 thermodynamic properties of aqueous species were calculated at elevated pressures and
163 temperatures using the Helgeson-Kirkham-Flowers (HKF) semi-empirical EoS model (Helgeson
164 et al., 1981; Shock et al., 1992; Shock and Helgeson, 1988; Tanger and Helgeson, 1988).

Thermodynamic properties of water were calculated by the Haar-Gallagher-Kell EoS (Kestin et al., 1984). The standard state adopted for aqueous species was that of a 1 molal solution referenced at infinite dilution. The MINES thermodynamic database (Gysi et al., 2023) was used as the source for the properties of aqueous species and minerals (Tables 1 and 2), which were extended in the present study with the properties of rhabdophane (Table 3).

The aqueous species properties implemented in GEMS include the HKF EoS parameters and the standard partial molal properties for aqueous species at the reference temperature of 298.15 K and pressure of 1 bar (Table S1 in the supplementary data). These are the standard Gibbs energy and enthalpy of formation from the elements (i.e., $\Delta_f G^\circ_{298}$ and $\Delta_f H^\circ_{298}$), absolute entropy (S°_{298}), and volume (V°_{298}) of aqueous species sourced from the slop98.dat database (Haas et al., 1995; Shock et al., 1997; Sverjensky et al., 1997). The latter was implemented with the corresponding HKF parameters in the SUPCRT92 program (Johnson et al., 1992), and is hereafter referred to as Supcrt92. The thermodynamic properties for REE hydroxyl complexes are from Haas et al. (1995), who make use of theoretical extrapolations to high temperatures based on the available low-temperature experimental data at the time of data compilation. To date, this is still the only comprehensive dataset for all of the REE hydroxyl complexes which are revised in this study. Other REE aqueous species implemented in the MINES database (Gysi et al., 2023) include the $REECl^{2+}$ and $REECl_2^+$ species from the experimental study of Migdisov et al. (2009).

The standard molar thermodynamic properties of monazite and xenotime as well as their heat capacity (*Cp*) functions implemented in the MINES database (Gysi et al., 2023) are based on calorimetric measurements. These include $\Delta_f H^\circ_{298}$ data for all REE phosphate endmembers from Ushakov et al. (2001) and other selected data sources listed in Table 2 and the supplementary data (Table S2). The standard Gibbs energy of monazite/xenotime endmembers is calculated in GEMS at elevated temperature by using a 3-term *Cp* temperature integration function. Pressure is corrected assuming a constant molar volume of V°_m which is minimal at *swvp*, with the molar volume data taken from the X-ray diffraction study of Ni et al. (1995). Comparison of the values compiled in Table 2 to the Gibbs energy values reported by Navrotsky et al. (2015) in Table S2 indicates some differences depending on the source of data used for entropy and enthalpy combined with the enthalpy values reported by Ushakov et al. (2001). However, our reported Gibbs energy values are generally within the reported uncertainty of the data compiled by Navrotsky et al. (2015), except for $PrPO_4$, $EuPO_4$, $GdPO_4$, and $DyPO_4$. The latter are generally caused by the choice of enthalpy and entropy values. For internal consistency we have used the enthalpy values from Ushakov et al. (2001) for all the REE phosphate endmembers.

The thermodynamic properties of rhabdophane (La to Gd endmembers; Table 3) were taken from the solubility experiments of Gausse et al. (2016) conducted between 25 and 90 °C. The H_2O contents in rhabdophane molecules and their cell volumes were taken from Shelyug et al. (2018). These data were implemented in the MINES thermodynamic database (Gysi et al., 2023) as reaction- dependent components, i.e., solubility constants (K_{sp}) for the rhabdophane dissolution reaction according to:

$$REEPO_4 \cdot nH_2O(s) = REE^{3+}(aq) + PO_4^{3-}(aq) + nH_2O \quad (1)$$

$$K_{sp}(Rab) = a(REE^{3+}) \times a(PO_4^{3-}) \times a(H_2O)^n \quad (2)$$

The K_{sp} values from the solubility study of Gausse et al. (2016) were then used to retrieve the standard thermodynamic properties of rhabdophane at a reference temperature of 298.15 K and pressure of 1 bar (Table 3).

The activity coefficients (γi) of charged aqueous species were calculated using the extended Debye-Hückel equation (Robinson and Stokes, 1968),

$$log\gamma_i = \frac{A \cdot z_i^2 \cdot \sqrt{I}}{1 + B \cdot \mathring{a} \cdot \sqrt{I}} + \Gamma\gamma + b\gamma \cdot I \quad (3)$$

where A and B are the Debye-Hückel solvent parameters (Helgeson et al., 1981); å represents the ion size parameter, which is set to a constant value of 3.72 for the NaCl background electrolyte model by Helgeson et al. (1981), and else individual parameters were used from Kielland (1937); z_i is the charge of the i^{th} ion; b_γ is the extended term parameter; I is the ionic strength; Γ_γ is a mole fraction to the molality conversion factor. The b_γ value is an empirical parameter calculated as a function of temperature and pressure in GEMS (TSolMod library; Wagner et al. 2012) for the NaCl background electrolyte model by Helgeson et al. (1981), whereas the b_γ value for experiments conducted in perchloric acid ($HClO_4$) was set to 0.21 based on the hydrothermal experiments by Migdisov and Williams-Jones (2007).

2.2. Experimental solubility data and selection procedure

A comprehensive experimental database was compiled (Table S3 in the supplementary data) from available experimental REE phosphate solubility data (Byrne and Kim, 1993; Cetiner et al., 2005; Firsching and Brune, 1991; Gausse et al., 2016; Gysi et al., 2015, 2018; Gysi and Harlov, 2021; Jonasson et al., 1985; Liu and Byrne, 1997; Poitrasson et al., 2004; Pourtier et al., 2010; Rai et al., 2003; Van Hoozen et al., 2020). A workflow chart (Fig. S1) introduces the compilation and selection of experimental data and the thermodynamic parameter optimization procedure (described further below). The solubility data selected comprise temperature and

pressure, the type of experiments, the REE phosphate characterized, the composition of the experimental solutions (i.e., pH and dissolved cations and anion concentrations), the logK_{sp} values at given temperatures, and approach to equilibrium from under- or over-saturation (Table S3). Some of these data were excluded from the thermodynamic data optimization procedure due to the following reason(s): i) lack of characterization of starting or precipitated solid phases (i.e., monazite vs. rhabdophane), or solution compositions, or no report of dissolved phosphorus (P) concentration; ii) no evidence for attainment of equilibrium or relatively short experimental run times; iii) experimental data whose values are 2 orders of magnitude higher/lower than all other results at equal experimental conditions; iv) experimental conditions are beyond the studied range (e.g., temperatures >300 °C).

Particular attention was paid to the solubility data collected at temperatures <90 °C because metastable rhabdophane controls the solubility of REE phosphates at these conditions (de Kerdaniel et al., 2007; Roncal-Herrero et al., 2011; Gausse et al., 2016). The latter commonly has a higher measured solubility than monazite, which created some confusion in the literature as summarized by Gysi et al. (2018). The low temperature (<90 °C) solubility data with no clear mineral characterization (Byrne and Kim, 1993; Firsching and Brune, 1991; Jonasson et al., 1985; Liu and Byrne, 1997; Rai et al., 2003) were compared with our study but not included in the data optimization procedure. The experimental solubility data from Rai et al. (2003) and Pourtier et al. (2010) were not included in the parameter optimization because they either do not report P concentration and/or the experimental temperatures are higher than 300 °C. The monazite-(Nd) measured at 150 °C and xenotime-(Y) solubility data measured at <100 °C by Cetiner et al. (2005) were not included in the optimizations due to the extremely low solubility products reported (~2 orders of magnitude lower). Some other solubility studies (Byrne and Kim, 1993; Firsching and Brune, 1991; Jonasson et al., 1985; Liu and Byrne, 1997) don't have enough detailed experimental descriptions or do not contain the information necessary for importing and calculating speciation in GEMSFITS, and therefore, these data were also excluded from the optimizations. Nevertheless, their reported logK_{sp} values reported at 25 °C are used for comparison to other experimental studies.

2.3. Experimental REE database (ThermoExp_REE) and data categorization

The compiled experimental solubility data from Table S3 were further reformatted and imported into GEMSFITS. This new experimental database "ThermoExp_REE" can be found in the supplementary data as a .csv file, with a summary overview of selected data given in Table 4. This formatted table mainly contains four parts of information: i) the initial experimental

conditions (i.e., temperature, pressure, starting fluid compositions, and mineral equilibrated with); ii) the analytical results from the quenched experimental solutions (i.e., REE and P concentrations, and pH measured at 25 °C); iii) additional constraints including metastability constraints to model perchlorate vs. hydrochloric acid based aqueous solutions; iv) activity speciation models and their extended term parameters.

The selected experimental REE phosphate solubility data implemented in the current version of the ThermoExp_REE experimental database cover temperatures from 25 to 300 °C at *swvp* or pressure of 1 bar, pH values ranging between 0 and 2, aqueous solutions containing either NaCl/HCl or $HClO_4$/$NaClO_4$, and experimental studies that confirmed the nature of the REE phosphate phase(s) (i.e., hydrous rhabdophane/churchite or anhydrous monazite/xenotime) used in the experiments. Note that no solubility experiments conducted at > 300 °C and pH values > 2 were selected in the study due to the limited availability of experiments at those conditions. The solubility data selected for parameter optimization and speciation calculation were then subdivided into three groups based on the identified solids (i.e., rhabdophane, monazite, and xenotime) controlling solubility at given temperatures (Table 4).

At temperatures below 100 °C, rhabdophane solubility data by Cetiner et al. (2005), Gausse et al. (2016), and Poitrasson et al. (2004) were selected for the optimization procedure. Rhabdophane solubility data cover the temperature range from 21 to 90 °C in acidic solutions with pH values ranging between 0.5 and 2 (Table 4). The only study reporting rhabdophane solubility data from both under-/over-saturation is the study of Gausse et al. (2016), which indicates that rhabdophane has a higher solubility than monazite. Because of the metastability issue for REE phosphates at low temperature, the data by Gausse et al. (2016) were considered the most reliable for evaluating the solubility of rhabdophane between 25 and 90 °C. The low temperature La and Nd phosphate solubility data from the studies by Cetiner et al. (2005) and Poitrasson et al. (2004) were not included in the optimizations of rhabdophane because the solids used were characterized as monazite. No churchite solubility data were included in the parameter optimization due to no available solubility experiments. Gausse et al. (2016) carried out rhabdophane-(La to Gd) solubility and precipitation experiments from 25 to 90 °C in HCl-bearing aqueous solutions with pH values ranging between 0.5 and 1. Cetiner et al. (2005) carried out the rhabdophane-(Sm) solubility experiment at temperatures between 23 and 50 °C in NaCl-HCl- or $NaClO_4$-$HClO_4$-bearing solutions with pH values ranging between 1 and 2. Poitrasson et al. (2004) obtained rhabdophane-(Gd) solubility data at 21 °C in HCl-bearing aqueous solutions with a pH of 2.

The solubility data of LREE and HREE phosphates whose solubility experiments were measured at ≥100 °C are grouped into monazite and xenotime, respectively. Monazite solubility data cover temperatures between 21 and 300 °C in acidic solutions with pH values ranging between 0 and 2 (Table 4). Gysi et al. (2018) and Van Hoozen et al. (2020) systematically measured the solubility of all the monazite endmembers (La to Gd) from 100 to 250 °C using synthetic mm-sized monazite crystals in $HClO_4$-H_3PO_4-bearing aqueous solutions with a pH of 2. Poitrasson et al. (2004) conducted monazite-(Nd) solubility experiments from 200 to 300 °C at pH 2 in HCl-bearing aqueous solutions. The study by Poitrasson et al. (2004) used synthetic powder samples characterized by the monazite structure. Solubility data compiled for all the xenotime endmembers (Tb to Lu, and Y) are based on the experiments conducted in acidic solutions at temperatures between 100 and 300 °C (Table 4). Gysi et al. (2015) and Gysi and Harlov (2021) measured the solubility of all the xenotime endmembers using synthetic mm-sized xenotime crystals from 100 to 250 °C in $HClO_4$-H_3PO_4-bearing solutions at pH of 2.

2.4. Thermodynamic parameter optimization using GEMSFITS

The GEMSFITS code (Miron et al., 2015; http://gems.web.psi.ch/GEMSFITS) was used for optimizing the $\Delta_f G^\circ_{298}$ and $\Delta_f H^\circ_{298}$ values of REE aqueous species following an approach similar to Miron et al. (2016, 2017). GEMSFITS uses a set of input compositions from the compiled ThermoExp_REE experimental database file (ThermoExp_REE.csv in the supplementary data) which allows sequentially calculating equilibrium speciation for given pressure, temperature, and composition, followed by optimization of the $\Delta_f G^\circ_{298}$ values of selected REE aqueous species. The enthalpy of formation ΔH°_{298} can be recalculated from the optimized $\Delta_f G^\circ_{298}$ and fixed $\Delta_f S^\circ_{298}$ values in order to avoid breakage of internal consistency. The selected thermodynamic parameters (Cp°, ΔS°, and ΔH°) for REE phosphates can be obtained from calorimetry experiments. The data output from the equilibrium speciation calculations (i.e., REE and P concentrations, and pH values) are then compared to the measured experimental values (i.e., from solubility data), and the $\Delta_f G^\circ_{298}$ values are optimized until GEMSFITS converges to a minimum difference between measured input and calculated output values using the bound optimization by quadratic approximation (Powell, 2009). The composite scaled sensitivities (CSS) is one of the key optimization results indicating the sensitivity of a parameter to the experimental observations (Miron et al., 2015; Tiedeman and Hill, 2007). The global fitting algorithm is used for parameter optimization and permits deriving uncertainties in the optimized Gibbs energy values

via Monte Carlo simulations (Miron et al., 2015). Upper and lower bounds designed to constrain the calculation range of the $\Delta_f G^\circ_{298}$ values are set during the optimization (~10–30 kJ/mol).

The GEMS3K kernel (Kulik et al., 2013) is used for equilibrium speciation calculations with GEMSFITS, and solves the equilibrium problem using Gibbs energy minimization. Here we use GEMSFITS to evaluate the $\Delta_f G^\circ_{298}$ values of the dominant REE aqueous species in acidic fluids based on the conditions reported in the REE phosphate solubility experiments selected for thermodynamic data optimizations (Table 4). The HKF EoS parameters were fixed during the optimization calculations, but consequently, the solubility data for monazite/rhabdophane had to be subdivided into two temperature ranges (low temperature: 25–100 °C; high temperature: 100–300 °C) to optimize the parameters for LREE phosphates and to fit adequately the experimental solubility data from Table 4. For the HREE phosphate xenotime, the parameter optimization was conducted in the high-temperature range (100–300 °C), following the selection criteria presented in Fig. S1. Equilibrium speciation calculations using the GEMS code package (Kulik et al., 2013; Wagner et al., 2012) indicate that REE^{3+} and $REEOH^{2+}$ are the dominant REE aqueous species controlling the solubility of REE phosphates in acidic perchlorate-based aqueous solutions (this study and Gysi et al., 2018), and REE^{3+} and REE chlorides dominate in acidic NaCl/HCl-bearing solutions (Cetiner et al., 2005; Poitrasson et al., 2004). Since the properties of REE chloride species have been determined experimentally at elevated temperatures (Migdisov et al., 2009), we fixed their properties and only optimized the properties for REE^{3+} and REE hydroxyl complexes.

Three different fits were used to re-evaluate the solubility experiments included in the ThermoExp_REE database: 1) optimization of both REE^{3+} and $REEOH^{2+}$ species (FIT 1); 2) optimization of only REE^{3+} (FIT 2); 3) optimization of only $REEOH^{2+}$ (FIT 3). Optimization tests conducted for other minor REE hydroxyl species (i.e., $REE(OH)_2^+$, $REE(OH)_3^0$, $REE(OH)_4^-$) indicate that these species do not considerably affect the calculated REE solubility at the acidic experimental conditions. Hence, the standard Gibbs energies for these minor species were preliminarily fixed, where necessary by reaction constraints using the calculated formation constants reported by Haas et al. (1995) with the following reactions:

In FIT 1 and 2:

$$REE^{3+} + 2H_2O = 2H^+ + REE(OH)_2^+ \quad (4)$$

$$REE^{3+} + 3H_2O = 3H^+ + REE(OH)_3^0 \quad (5)$$

$$REE^{3+} + 4H_2O = 4H^+ + REE(OH)_4^- \quad (6)$$

In FIT 3:

$$REEOH^{2+} + H_2O = H^+ + REE(OH)_2^+ \quad (7)$$

$$REEOH^{2+} + 2H_2O = 2H^+ + REE(OH)_3^0 \quad (8)$$

$$REEOH^{2+} + 3H_2O = 3H^+ + REE(OH)_4^- \quad (9)$$

3. Results

3.1. Comparison of solubility data from experiments vs. calculated Supcrt92 predictions

Experimental data collected and predicted solubility products ($\log K_{sp}$) derived from our new data compilation (Table S3) are shown as a function of $10^3/T$ (T is the temperature in Kelvin) from 25 to 300 °C in Figs. 1 and 2 for rhabdophane, monazite, and xenotime solubility. The calculated Supcrt92 predictions are shown as initial "Predictions without Optimization" in the workflow chart in Fig. S1. The predicted log*K*sp values are calculated using the existing HKF parameters and thermodynamic data from the Supcrt92 database for aqueous species (Table S1) combined with the calorimetric data for minerals (Tables 2 and 3). The experimental solubility data were taken from the log*K*sp values reported in previous studies (Byrne and Kim, 1993; Cetiner et al., 2005; Firsching and Brune, 1991; Gausse et al., 2016; Gysi et al., 2018; Gysi and Harlov, 2021; Jonasson et al., 1985; Liu and Byrne, 1997; Poitrasson et al., 2004; Rai et al., 2003; Van Hoozen et al., 2020). The log*K*sp values reported from these solubility studies are listed in Table S4. The results show that, for both monazite and xenotime, the predicted log*K*sp values from Supcrt92 combined with the calorimetric properties of minerals generally under-predict the solubility of REE phosphates in comparison to the experimentally derived solubility products for most of the endmembers (Figs. 1 and 2). The predicted $\log K_{sp}$ values <90 °C for the metastable rhabdophane phase are 0.5–3 orders of magnitude higher than monazite, but both phases display an overall retrograde solubility, i.e. decreasing solubility with increased temperature (Fig. 1). The predicted log*K*sp values of monazite are 0.5–2 orders of magnitude smaller than the experimental solubility data, except for the solubility of monazite-(La) and -(Ce) matching closely the experimental data (Fig. 1). These discrepancies slightly increase with temperature. The predicted solubility of rhabdophane is in better agreement with the experimental solubility data (Fig. 1), except for rhabdophane-(Eu) exhibiting up to 1 order of magnitude higher predicted log*K*sp values (Fig. 1f). The predicted log*K*sp values of xenotime are up to 4 orders of magnitude lower than the experimental values (Fig. 2), except for xenotime-(Tm, Yb, and Lu), which are in closer agreement. The xenotime solubility data derived by Gysi et al. (2015) and Gysi and Harlov (2021) between

100 and 250 °C match with the lower temperature solubility data from previous studies (Byrne and Kim, 1993; Firsching and Brune, 1991; Jonasson et al., 1985; Liu and Byrne, 1997).

The solubility of Nd and Er phosphates is shown in Fig. 3 to inspect the total dissolved REE molalities and the typical speciation behavior of REE aqueous species that control the solubility of monazite, rhabodphane, and xenotime between 25 and 300 °C. Speciation calculations using *a priori* (before optimization) the Supcrt92 dataset, indicate that the two species that control REE solubility in perchloric acid-based aqueous solutions (pH of 2) are REE^{3+} and $REEOH^{2+}$; the latter becoming more important with increasing temperature. For the solubility of rhabdophane, REE^{3+} is the dominant aqueous species controlling its solubility at <90 °C and at pH of 1 in HCl acid solutions (Fig. 3a). Other REE species, including the REE chloride in the HCl-bearing acid solutions, have activities at least 2 orders of magnitude lower, and therefore are not considered to affect significantly the solubility calculations and thermodynamic data optimizations in these acidic solutions in the temperature range of the experiments reviewed in this study. We must therefore conclude that the large discrepancies observed between experimental solubility data and calculated predictions using Supcrt92 result from problematic thermodynamic data for the REE^{3+} and $REEOH^{2+}$ aqueous species.

3.2. Resolving discrepancies between experiments and predicted REE phosphate solubilities: GEMSFITS optimization of $\Delta_f G°_{298}$

There are large discrepancies between the experimental REE phosphate solubility data and the calculated predictions based on the aqueous species from the Supcrt92 dataset (Figs. 1–3). These discrepancies can, however, be resolved through optimization of the $\Delta_f G^\circ_{298}$ values of REE^{3+} and/or $REEOH^{2+}$ using GEMSFITS to reconcile the experimental solubility data from the ThermoExp_REE database and calculated solubilities at each experimental condition (summarized in Table 4). The optimization procedure and fitting trials (FIT 1–3) are presented in the workflow chart in Fig. S1.

As mentioned above, three different parameter fits (FIT 1: REE^{3+} and $REEOH^{2+}$; FIT 2: REE^{3+}, FIT 3: $REEOH^{2+}$) were tested to determine the best fits for monazite and xenotime at temperatures ≥100 °C. Only FIT 2 was used for rhabdophane at temperatures <100 °C because its solubility is controlled by the REE^{3+} species (Fig. 3). The initial $\Delta_f G^\circ_{298}$ and newly optimized $\Delta_f G^\circ_{298}$ values and their associated uncertainties are listed for all REE aqueous species and the three fitting methods in Tables 5 (data <100 °C) and 6 (data ≥100 °C). The effect of each of these

optimizations can be further inspected in Fig. 4 for the solubility of monazite, in Fig. 5 for the solubility of xenotime, and in Fig. 6 for the solubility of rhabodphane.

For the optimizations at ≥100 °C, FIT 1 results in an excellent fit to the experimental solubility data for both, the LREE (La to Gd; monazite) and HREE (Tb to Lu, and Y; xenotime) phosphates, which can be illustrated in a logarithm REE molalities vs. temperature diagram (Figs. 4 and 5). These diagrams show the experimental solubility data and the re-calculated solubilities of monazite and xenotime using the optimized $\Delta_f G^\circ_{298}$ values generated from GEMSFITS. The CSS values in Tables 5 and 6 are an indicator of the sensitivity of a parameter to the experiments. Inspecting the CSS values of optimization FIT 1, indicates that both REE species, $LREE^{3+}$ and $LREEOH^{2+}$, are generally within the same scale, whereas the CSS values for $HREEOH^{2+}$ are very small or close to zero (i.e., ~2 orders of magnitude lower). Therefore, the $\Delta_f G^\circ_{298}$ values data that need to be optimized include both LREE species (i.e., $LREE^{3+}$ and $LREEOH^{2+}$) in order to reproduce the experimental solubility data of monazite. This is also illustrated by the poor fits to the solubility data when optimizations FIT 2 or 3 are used (Fig. 4). In contrast, only the $\Delta_f G^\circ_{298}$ values of the $HREE^{3+}$ species needs to be optimized in order to reproduce the experimental xenotime solubility data. This is illustrated by both optimizations FIT 1 and 2 overlapping closely with the experimental solubility data, and optimization FIT 3 failing to reproduce the experimental data (Fig. 5). Similarly, the optimization of $\Delta_f G^\circ_{298}$ values of the $LREE^{3+}$ species by FIT 2 was sufficient to accurately predict the rhabdophane solubility at T <100 °C (Fig. 6). Overall, the necessary adjustments of $\Delta_f G^\circ_{298}$ values are significant. For accurate predictions of the solubility of rhabdophane, $\Delta_f G^\circ_{298}$ values of $LREE^{3+}$ need to be adjusted by ~1–6 kJ/mol (Table 5; Fig. S2); for monazite solubility, $\Delta_f G^\circ_{298}$ values of $LREE^{3+}$ need to be adjusted by ~2–10 kJ/mol and $LREEOH^{2+}$ by ~13–30 kJ/mol (Table 6; Fig. S2). For accurate predictions of the solubility of xenotime, $\Delta_f G^\circ_{298}$ values of $HREE^{3+}$ need to be adjusted by ~10–26 kJ/mol (Table 6; Fig. S2).

Monazite-(Nd) and xenotime-(Er) are used as representative examples in Fig. 7 to show how aqueous speciation is affected by the optimizations described above, and how the fits improve the predicted REE phosphate solubilities. Both Nd^{3+} and $NdOH^{2+}$ control the solubility of monazite-(Nd) but their relative weighting depends on temperature (Fig. 7a). The steeper slope at <150 °C in a logarithm Nd molality vs. temperature diagram is controlled by the stability of the Nd^{3+} species, whereas the flatter slope at >150 °C is controlled by the stability of the $NdOH^{2+}$ species. In contrast, the solubility of xenotime is dominantly controlled by the stability of the $HREE^{3+}$ species, which results in the observed steep slope in this diagram (Fig. 7b). The same observations are applicable to the solubility of other monazite and xenotime endmembers.

4. Discussion

4.1. Fitted REE phosphate solubility products between 25−300 °C and comparison to experimental solubility studies

The corrections of $\Delta_f G^\circ_{298}$ values for REE^{3+} and $REEOH^{2+}$ aqueous species are significant (Tables 5 and 6) but necessary with the current optimization approach in order to keep the optimized dataset internally consistent with the HKF parameters for aqueous species. The recommended optimizations (FIT 1 for monazite; FIT 2 for xenotime and rhabdophane) allow to accurately predict the solubility of all of the REE phosphates in acidic solutions (Figs. 4–7) but can also be re-evaluated in the future as more data become available for the experimental database (ThermoExp_REE in the supplementary data). Considering how well the experimental solubility data are now predicted using the optimized REE aqueous species derived in our study, we provide here a set of recommended $\log K_{sp}$ values which were fitted between 25 and 300 °C with the coefficients and $\log K_{sp}$ values at reference conditions (298.15 K and 1 bar) listed in Table 7.

Figures 8 and 9 show a comparison between calculated $\log K_{sp}$ values for all of the REE phosphates as a function of temperature and the re-calculated experimental $\log K_{sp}$ values based on the optimized thermodynamic data for REE aqueous species derived in our study. The solubility data that were re-calculated are based on the experimental data by Cetiner et al. (2005), Gausse et al. (2016), Gysi et al. (2015, 2018), Gysi and Harlov (2021), Poitrasson et al. (2004), and Van Hoozen et al. (2020). Figure 8 shows that the optimized $\log K_{sp}$ values for rhabdophane and monazite endmembers display an overall better agreement with the experimental data in comparison to the calculated values using Supcrt92, which under-predicts monazite solubility. It is also worth noting that most of the rhabdophane endmembers display a distinctly higher solubility than monazite at 25 °C. Furthermore, the reported room temperature $\log K_{sp}$ values derived in previous studies (Byrne and Kim, 1993; Firsching and Brune, 1991; Jonasson et al., 1985; Tananaev and Vasil'eva, 1963), whose starting REE phosphate powders were not characterized, seem to be more consistent with the optimized solubility products of rhabdophane rather than monazite (Fig. 8). The predicted $\log K_{sp}$ values for xenotime are all in excellent agreement with both the low- and high- temperature solubility data by Firsching and Brune (1991), Gysi et al. (2015), and Gysi and Harlov (2021), whereas Supcrt92 significantly under-predict the experimental solubility data for most of the xenotime endmembers (Fig. 9). We also notice that the Supcrt92 predictions of monazite-(La and Ce) solubilities and xenotime-(Yb and Lu) are better than the rest of monazite and xenotime endmembers, respectively (Figs. 8 and 9). This is possibly

caused by the HKF parameters of the REE aqueous ions that were derived previously based on available low temperature experimental data which causes those parameters to have poor extrapolations to elevated temperatures.

The logK_{sp} values of all monazite and xenotime endmembers were calculated between 100 and 300 °C from the fitted coefficients in Table 7 and are compared to each other in Fig. 10 as a function of the REE ionic radii. The logK_{sp} values derived from solubility experiments were re-evaluated by re-calculating their equilibrium speciation in GEMSFITS and using the optimized $\Delta_f G^\circ_{298}$ values from Table 6. Overall, the optimized log$K$sp values of all monazite endmembers are very similar for all isotherms up to 300 °C and their solubilities are lower than xenotime (Fig. 10). There is a noticeable decrease in log$K$sp values with decreased REE ionic radii from monazite-(La) to -(Sm). In contrast, there is an increase in log$K$sp values from monazite-(Sm) to -(Gd) as well as from xenotime-(Tb) to (Y) for all isotherms and decreasing ionic radii of the REE. Finally, xenotime-(Y) to -(Lu) display an overall decrease in solubility with smaller REE ionic radii.

4.2. REE phosphate solubility products at reference conditions (298.15 K and 1 bar)

Figure 11 shows a comparison between the optimized logK_{sp} values at reference conditions and the literature values (Table S4). The logK_{sp} values of monazite (La, Nd, Sm, and Gd) reported by Cetiner et al. (2005) and Poitrasson et al. (2004) are 0.5 to 3 orders of magnitude higher than our results. Their extrapolated values at reference conditions are closer to the measured solubility of metastable rhabdophane because of its solubility control in experiments conducted at these low temperatures. Indeed, all of the solubility data of rhabdophane determined by Gausse et al. (2016) from under- and oversaturation are systematically higher than the monazite solubility experiments conducted between 100 and 250 °C and extrapolated down to reference conditions in the experiments by Gysi et al. (2015, 2018), Gysi and Harlov (2021), and Van Hoozen et al. (2020). These observations are also in line with our optimized solubility data at reference conditions which are internally consistent with the before mentioned experimental studies, and justifies splitting the optimizations into low and high temperature datasets (Tables 5 and 6). We therefore do not recommend the use of these other solubility data because of the resulting high variability in measured solubility at <100 °C due to the rhabdophane metastability at those conditions. This is illustrated by the variability of logK_{sp} values determined in the studies by Firsching and Brune (1991), Liu and Byrne (1997), Rai et al. (2003), and Tananaev and Vasil'eva (1963) spanning a range of values between monazite and rhabdophane (Fig. 11).

The optimized logK_{sp} values for rhabdophane are generally in line with the values by Gausse et al. (2016), but ~0.5–2 orders of magnitude lower than the values by Byrne and Kim (1993), and ~0.5–1 order of magnitude higher than the results by Firsching and Brune (1991) and Liu and Byrne (1997). The optimized logK_{sp} value of rhabdophane-(La) are similar to the values derived by Byrne and Kim (1993), Cetiner et al. (2005), Jonasson et al. (1985), Rai et al. (2003), and Tananaev and Vasil'eva (1963). The optimized logK_{sp} value of rhabdophane-(Gd) is close to the values derived by Tananaev and Vasil'eva (1963), and rhabdophane-(Nd) is close to the logK_{sp} values derived by Byrne and Kim (1993), Cetiner et al. (2005), and Jonasson et al. (1985).

The optimized logK_{sp} values of xenotime derived in our study are in agreement with most of the literature values derived at low temperature including data by Byrne and Kim (1993), Firsching and Brune (1991), Jonasson et al., (1985), and Liu and Byrne (1997); except the data for xenotime-(Ho) and -(Lu) endmembers, whose logK_{sp} values are about 0.5–1 order of magnitude higher in comparison to our study. Furthermore, the optimized logK_{sp} values of xenotime are in close agreement with most of the values retrieved in the 100−250 °C solubility experiments by Gysi et al. (2015) and Gysi and Harlov (2021).

We note here that the optimization method presented in our study results in some deviations from the systematic pattern observed for logK_{sp} (25 °C and 1 bar) values as a function of REE ionic radii derived in other studies (Fig. 11). The cause of these deviations is mainly the optimization approach which assumes only a correction of $\Delta_f G^\circ_{298}$ values for aqueous species without including any optimizations for the solids. Indeed, the largest discrepancies in logK_{sp} values at 25 °C and 1 bar are observed for La, Pr, Nd, Eu, Dy, Y, and Tm which can display between 0.5 to 1 logK_{sp} units differences in comparison to the logK_{sp} values extrapolated to reference conditions in the solubility studies by Gysi et al. (2015), Van Hoozen et al. (2020), and Gysi and Harlov (2021). This calls for a need for more experimental data to verify the properties of the HKF parameters derived for the REE^{3+} aqua ions and used in the present study as a fixed parameter in the optimization method.

4.3. Implication of the optimizations for modeling the solubility and speciation of REE

4.3.1. LREE vs. HREE species controlling the solubility of monazite and xenotime at hydrothermal conditions

In Fig. 12, the calculated solubilities of all of the monazite and xenotime endmembers are compared as a function of temperature before and after optimizations. This comparison indicates large observed differences in the predicted monazite and xenotime solubility behavior between 25

553 and 300 °C. In particular, the optimized REE phosphate solubilities indicate that monazite is more
554 soluble above 150 °C than predicted using Supcrt92, whereas xenotime displays higher solubilities
555 than monazite at <100 °C.
556 Comparison of the slopes in the logarithm molality REE versus temperature diagram (Fig.
557 12) further indicates that the REE species controlling solubility are significantly different from the
558 prediction using Supcrt92. The predicted monazite solubility slopes in Fig. 12a remain relatively
559 constant for all of the endmembers, and start flattening only at temperatures above 200−300 °C,
560 whereas the predicted xenotime solubility slopes are much flatter and constant in the whole
561 temperature range (Fig. 12a). In contrast to these predictions, the solubility slopes of monazite
562 flatten at temperatures above 150 °C based on our optimized thermodynamic dataset and the
563 solubility of xenotime displays a much steeper slope in a logarithm molality REE versus
564 temperature diagram (Fig. 12b). The main cause for the observed differences in solubility behavior
565 is the stability of the $LREE^{3+}$ and $LREEOH^{2+}$, with the former species controlling the steep
566 solubility slope of monazite at <150 °C and the latter species controlling the flat solubility slope
567 at >150 °C, respectively (Fig. 7). For all xenotime endmembers, the $HREE^{3+}$ species controls their
568 solubilities at temperatures between 25 and 300 °C, which is reflected in the near constant
569 solubility slopes in this temperature range (Fig. 12b).
570 The above observations strongly suggest that the HKF parameters derived in the study by
571 Haas et al. (1995) for the REE^{3+} species and REE hydroxyl complexes are highly inaccurate in the
572 temperature range considered. This results in an inaccurate interpretation of the role of REE^{3+} and
573 $REEOH^{2+}$ in controlling the solubility of REE phosphates. The optimized $HREE^{3+}$ species based
574 on xenotime solubility and the optimized $LREE^{3+}$ and $LREEOH^{2+}$ species based on monazite
575 solubility have both important implications for modeling the solubility and fractionation of REE
576 in acidic to mildly acidic fluids. In particular, the simulated solubility of monazite is now much
577 higher with increased temperature and the solubility of individual monazite and xenotime
578 endmembers show a much tighter distribution for both the LREE and HREE (Fig. 12). This will
579 result in a higher simulated mobility for the LREE over the HREE.
580

581 *4.3.2. Implications of the optimizations of REE^{3+} and $REEOH^{2+}$ species for the speciation of REE*
582 *as a function of pH*
583 Activities of REE aqueous species were calculated as a function of pH (2–9) at 250 °C to
584 determine the effects of the optimized $\Delta_f G^\circ_{298}$ values from Table 6 on the REE speciation
585 calculations. Figure 13 shows a typical example of these speciation calculations for Nd and Er;

other REE species can be found in Figs. S3 and S4. For all monazite and xenotime endmembers, the activities of REE^{3+} and $REEOH^{2+}$ decrease from acidic to mildly acid pH (2-6) and speciation is controlled sequentially by the $REE(OH)_2^+$, $REE(OH)_3^0$, and $REE(OH)_4^-$ species. The total molality of dissolved REE decreases first from pH 2 to 6 displaying a minimum at near neutral pH followed by an increase to alkaline pH values. Xenotime shows a similar overall behavior but with a minima observed at acidic pH of ~4. We should note that the modeling of the speciation and molality of REE species in perchloric acid was done to illustrate the differences before and after the optimization of REE^{3+} and $REEOH^{2+}$ instead of illustrating the change of REE molality with pH in natural hydrothermal fluids.

Figure 13a shows a comparison of Nd speciation using Supcrt92 and the optimized Nd^{3+} and $NdOH^{2+}$ species at 250 °C. This figure indicates that the activity of $NdOH^{2+}$ is significantly increased after the parameter optimization, whereas Nd^{3+} generally remains unchanged from pH 2 to 9, and other species ($Nd(OH)_3^0$, $Nd(OH)_4^-$ and $Nd(OH)_2^+$) generally remain the same in the pH range of 2–5 but are moderately increased in the pH range of 5–9. Hence, optimization of the Nd aqueous species results in a higher stability of the $NdOH^{2+}$ species in comparison to what was predicted from Supcrt92 which controls the solubility of monazite-(Nd) in acidic solutions. This optimization leads to an increased total Nd molality by 1 and 0.5 order of magnitude at pH <5 and >5, respectively, which is mainly caused by the increased $NdOH^{2+}$, $Nd(OH)_3^0$, and $Nd(OH)_4^-$ activities after the optimization. Similar speciation results can be found for the solubility of other monazite endmembers (Fig. S3). The increased $NdOH^{2+}$ predominance based on the optimized thermodynamic properties and REE phosphate solubility data compiled in our study are in line with the study by Pourtier et al. (2010) but conflicts with the experimental results reported by Wood et al. (2002), which indicate a higher stability of the Nd^{3+} aqua ion over the $NdOH^{2+}$ species. More experiments are needed to better constrain the properties of these REE hydroxyl species as a function of pH and temperature, which would aid in conducting improved optimizations of $\Delta_f G^\circ$ values at different temperatures and not only at reference conditions.

Figure 13b shows a comparison of Er speciation using Supcrt92 and the optimized Er^{3+} species at 250 °C. These optimizations result in an increased activity of all Er aqueous species, except $ErOH^{2+}$ which displays a decrease in activity because its $\Delta_f G^\circ_{298}$ value was fixed in FIT 2. After the optimization, the total Er molality is increased by 1 order of magnitude within the entire pH range. This is caused by the increased activities of Er^{3+}, $Er(OH)_2^+$, $Er(OH)_3^0$, and $Er(OH)_4^-$ predominating sequentially from pH 2 to 9. The major difference between the speciation calculations using Supcrt92 and optimized species is the considerable increase in Er^{3+} stability

controlling the solubility of xenotime-(Er) at pH <3 instead of the $ErOH^{2+}$ predicted by Supcrt92 (Fig. 13b). Similar speciation results are found for the other HREE (Fig. S4).

5. Conclusions

In this study, the $\Delta_f G^\circ_{298}$ values of $LREE^{3+}$ used at temperatures <100 °C (Table 5), and $LREE^{3+}$, $LREEOH^{2+}$, and $HREE^{3+}$ used at temperatures ≥100 °C (Table 6) are optimized using existing experimental REE phosphate solubility data. The results of the speciation calculations and parameter optimizations indicate that the solubility of both monazite and rhabdophane are controlled by REE^{3+} at temperatures below 150 °C with a switchover to $REEOH^{2+}$ at temperatures above 150 °C. In contrast, the solubility of xenotime is controlled by REE^{3+} in acidic solutions from 25 to 300 °C. The optimal match to rhabdophane solubility data requires modifying the $\Delta_f G^\circ_{298}$ values of $LREE^{3+}$ by 1–6 kJ/mol between 25 and 100 °C from those predicted by the Supcrt92 dataset. The optimal match to the monazite solubility data between 100 and 300 °C requires modifying the $\Delta_f G^\circ_{298}$ values for REE^{3+} by ~2–10 kJ/mol and $REEOH^{2+}$ by ~15–31 kJ/mol, respectively. For xenotime endmembers, optimizing only the $\Delta_f G^\circ_{298}$ values of REE^{3+} by 1–26 kJ/mol is sufficient to fit the experimental solubility data between 100 and 300 °C.

These optimized Gibbs energy values using GEMSFIT allow for the reconciliation of discrepancies between solubility measurements and predictions by the REE aqueous species from the Supcrt92 dataset and existing calorimetric data for minerals. The optimized $\Delta_f G^\circ_{298}$ for proposed aqueous species should be considered as provisional due to the uncertainty in the HKF EoS parameters, which were fixed in this study, and the limitation of selected or existing experimental solubility data (<300 °C and acidic pH). More solubility data are needed at high temperatures (e.g., >300 °C) and as a function of pH (e.g., pH >2) to reliably optimize the $\Delta_f G^\circ$ of REE species at each of the experimental temperatures and further develop a new temperature dependent EoS model for the REE. Moreover, some solubility experiments of other REE minerals (e.g., REE -oxides, -hydroxides, -sulfates, -fluorides, -chlorides, and carbonates) in various solutions (e.g., HCl, HF, and H_2SO_4 acids) need to be conducted at elevated temperatures. Nevertheless, the new experimental database for REE (ThermoExp_REE) and optimized thermodynamic datasets from Tables 5 and 6, are building a basic framework for future optimizations, extensions to other ligands, and implementations of new experimental data.

Declaration of Competing Interest

The authors declare that they have no known competing financial interests or personal relationships that could have appeared to influence the work reported in this paper.

Data availability

The experimental and thermodynamic data compiled and optimized in this study are provided in the supplementary material files.

Acknowledgments

This research was funded for experimental data compilation and thermodynamic optimizations by the U.S. Department of Energy, Office of Science, Office of Basic Energy Sciences, Geosciences program under Award Numbers DE-SC0022269 and DE-SC0021106 to AG. The initial review of mineral thermodynamic data was funded by the National Science Foundation Award Numbers NSF CAREER EAR-2039674 and EAR-2032761 to AG. We would like to also thank our colleagues for fruitful discussions and comments on the thermodynamic properties of REE, particularly D. Harlov, N. Hurtig, and D. Kulik. We are grateful to Weihua Liu, A. Migdisov, and two anonymous reviewers for their constructive comments. We also thank O. Pokrovsky for the editorial handling.

Appendix A. Supplementary data

Figures S1-S4

Tables S1-S4

ThermoExp_REE.csv

673 **References**

Andersen, A.K., Clark, J.G., Larson, P.B. Donovan, J.J., 2017. REE fractionation, mineral speciation, and supergene enrichment of the Bear Lodge carbonatites, Wyoming, USA. Ore Geol. Rev. 89, 780–807. https://doi.org/10.1016/j.oregeorev.2017.06.025

Bau, M., Dulski, P., 1999. Comparing yttrium and rare earths in hydrothermal fluids from the Mid-Atlantic Ridge: Implications for Y and REE behaviour during near-vent mixing and for the Y/Ho ratio of proterozoic seawater. Chem. Geol. 155, 77–90. https://doi.org/10.1016/S0009-2541(98)00142-9

Boatner, L.A., 2002. Synthesis, structure, and properties of monazite, pretulite, and xenotime. Rev. Mineral. Geochem. 48, 87–121. https://doi.org/10.2138/rmg.2002.48.4

Byrne, R.H., Kim, K.H., 1993. Rare earth precipitation and coprecipitation behavior: The limiting role of PO_4^{3-} on dissolved rare earth concentrations in seawater. Geochim. Cosmochim. Acta 57, 519–526. https://doi.org/10.1016/0016-7037(93)90364-3

Cetiner, Z.S., Wood, S.A., Gammons, C.H., 2005. The aqueous geochemistry of the rare earth elements. Part XIV. The solubility of rare earth element phosphates from 23 to 150 °C. Chem. Geol. 217, 147–169. https://doi.org/10.1016/j.chemgeo.2005.01.001

Cook, N.J., Ciobanu, C.L., O'Rielly, D., Wilson, R., Das, K., Wade, B., 2013. Mineral chemistry of Rare Earth Element (REE) mineralization, Browns Ranges, Western Australia. Lithos 172–173, 192–213. https://doi.org/10.1016/j.lithos.2013.04.012

Firsching, F.H., Brune, S.N., 1991. Solubility Products of the Trivalent Rare-Earth Phosphates. J. Chem. Eng. Data 36, 93–95. https://pubs.acs.org/doi/pdf/10.1021/je00001a028

Gausse, C., Szenknect, S., Qin, D.W., Mesbah, A., Clavier, N., Neumeier, S., Bosbach, D., Dacheux, N., 2016. Determination of the Solubility of Rhabdophanes $LnPO_4 \cdot 0.667H_2O$ (Ln = La to Dy). Eur. J. Inorg. Chem. 2016, 4615–4630. https://doi.org/10.1002/ejic.201600517

Gavrichev, K.S., Smirnova, N.N., Gurevich, V.M., Danilov, V.P., Tyurin, A.V., Ryumin, M.A., Komissarova, L.N., 2006. Heat capacity and thermodynamic functions of $LuPO_4$ in the range 0-320 K. Thermochim. Acta 448, 63–65. https://doi.org/10.1016/j.tca.2006.05.019

Gavrichev, K.S., Ryumin, M.A., Tyurin, A.V., Gurevich, V.M., Komissarova, L.N., 2008. Refined heat capacity of $LaPO_4$ in the temperature range 0-1600 K. Thermochim. Acta 474, 47–51. https://doi.org/10.1016/j.tca.2008.05.004

Gavrichev, K.S., Ryumin, M.A., Tyurin, A.V., Gurevich, V.M., Komissarova, L.N., 2009. The heat capacity and thermodynamic functions of $EuPO_4$ over the temperature range 0-1600 K. Russ. J. Phys. Chem. A 83, 901–906. https://doi.org/10.1134/S0036024409060053

Gavrichev, K.S., Ryumin, M.A., Tyurin, A.V., Gurevich, V.M. and Komissarova, L.N., 2010. Heat Capacity and Thermodynamic Functions of Xenotime YPO_4(c) at 0-1600 K. Geochem. Int. 48, 932–939. https://doi.org/10.1134/S0016702910090065

Gavrichev, K.S., Ryumin, M.A., Tyurin, A.V., Gurevich, V.M., Khoroshilov, A.V., Komissarova, L.N., 2012. Thermodynamic functions of erbium orthophosphate $ErPO_4$ in the temperature range of 0-1600 K. Thermochim. Acta 535, 1–7. https://doi.org/10.1016/j.tca.2012.02.002

Gavrichev, K.S., Ryumin, M.A., Khoroshilov, A.V., Nikiforova, G.E., Tyurin, A.V., Gurevich, V.M., Starykh, R.V., 2013a. Thermodynamic properties and phase transitions of tetragonal modification of terbium orthophosphate. Vestnik (Herald) of St. Petersburg State University 4, 186–197.

Gavrichev, K.S., Ryumin, M.A., Tyurin, A.V., Gurevich, V.M., Nikiforova, G.E., Komissarova, L. N., 2013b. Heat capacity and thermodynamic functions of $YbPO_4$ from 0 to 1800 K. Inorg. Mater. 49, 701–708. https://doi.org/10.1134/S0020168513070042

Gavrichev, K.S., Gurevich, V.M., Ryumin, M.A., Tyrin, A.V., Komissarova, L.N., 2016. Low-temperature heat capacity and thermodynamic properties of $PrPO_4$. Geochem. Int. 54, 362–368. https://doi.org/10.1134/S001670291602004X

Gysi, A.P., Hurtig, N.C., Pan, R., Miron, G.D., and Kulik, D.A., 2023, MINES thermodynamic database, New Mexico Bureau of Geology and Mineral Resources, version 19.1, https://doi.org/10.58799/mines-tdb

Gysi, A.P., Harlov, D., 2021. Hydrothermal solubility of $TbPO_4$, $HoPO_4$, $TmPO_4$, and $LuPO_4$ xenotime endmembers at pH of 2 and temperatures between 100 and 250 °C. Chem. Geol. 567, 120072. https://doi.org/10.1016/j.chemgeo.2021.120072

Gysi, A.P., Harlov, D., Miron, G.D., 2018. The solubility of monazite ($CePO_4$), $SmPO_4$, and $GdPO_4$ in aqueous solutions from 100 to 250 °C. Geochim. Cosmochim. Acta 242, 143–164. https://doi.org/10.1016/j.gca.2018.08.038

Gysi, A.P., Williams-Jones, A.E., 2013. Hydrothermal mobilization of pegmatite-hosted REE and Zr at Strange Lake, Canada: A reaction path model. Geochim. Cosmochim. Acta 122, 324–352. https://doi.org/10.1016/j.gca.2013.08.031

Gysi, A.P., Williams-Jones, A.E., 2015. The thermodynamic properties of bastnäsite-(Ce) and parisite-(Ce). Chem. Geol. 392, 87–101. https://doi.org/10.1016/j.chemgeo.2014.11.001

Gysi, A.P., Williams-Jones, A.E., Collins, P., 2016. Lithogeochemical vectors for hydrothermal processes in the Strange Lake peralkaline granitic REE-Zr-Nb deposit. Econ. Geol. 111, 1241–1276. https://doi.org/10.2113/econgeo.111.5.1241

Gysi, A.P., Williams-Jones, A.E., Harlov, D., 2015. The solubility of xenotime-(Y) and other HREE phosphates ($DyPO_4$, $ErPO_4$ and $YbPO_4$) in aqueous solutions from 100 to 250°C and psat. Chem. Geol. 401, 83–95. https://doi.org/10.1016/j.chemgeo.2015.02.023

Haas, J.R., Shock, E.L., Sassani, D.C., 1995. Rare earth elements in hydrothermal systems: Estimates of standard partial molal thermodynamic properties of aqueous complexes of the rare earth elements at high pressures and temperatures. Geochim. Cosmochim. Acta 59, 4329–4350. https://doi.org/10.1016/0016-7037(95)00314-P

Harlov, D.E., Meighan, C.J., Kerr, I.D., Samson, I.M., 2016. Mineralogy, Chemistry, and Fluid-Aided Evolution of the Pea Ridge Fe Oxide-(Y+REE) Deposit, Southeast Missouri, USA. Econ. Geol. 111, 1963–1984. https://doi.org/10.2113/econgeo.111.8.1963

Helgeson, H.C., Kirkham, D.H., 1974. Theoretical prediction of the thermodynamic behavior of aqueous electrolytes at high pressures and temperatures; II, Debye-Huckel parameters for activity coefficients and relative partial molal properties. Am. J. Sci. 274, 1199–1261.

Helgeson, H.C., Kirkham, D.H., Flowers, G.C., 1981. Thermodynamic behavior of aqueous electrolytes at high pressure and temperature. Am. J. Sci. 281, 1249–1516.

Hingerl, F.F., Kosakowski, G., Wagner, T., Kulik, D.A., Driesner, T., 2014. GEMSFIT: A generic fitting tool for geochemical activity models. Comput. Geosci. 18, 227–242. https://doi.org/10.1007/s10596-014-9405-3

Holland, T.J.B., Powell, R., 1998. An internally consistent thermodynamic data set for phases of petrological interest. J. Metamorph. Geol. 16, 309–343. https://doi.org/10.1111/j.1525-1314.1998.00140.x

Huang, Y., He, H., Liang, X., Bao, Z., Tan, W., Ma, L., Zhu, J., Huang, J., Wang, H., 2021. Characteristics and genesis of ion adsorption type REE deposits in the weathering crusts of metamorphic rocks in Ningdu, Ganzhou, China. Ore Geol. Rev. 135. https://doi.org/10.1016/j.oregeorev.2021.104173

Hurtig, N.C., Hanley, J.J., Gysi, A.P., 2018. The role of hydrocarbons in ore formation at the Pillara Mississippi Valley-type Zn-Pb deposit, Canning Basin, Western Australia. Ore Geol. Rev. 102, 875–893. https://doi.org/10.1016/j.oregeorev.2018.09.012

Ji, Y., Beridze, G., Bosbach, D., Kowalski, P.M., 2017. Heat capacities of xenotime-type ceramics: An accurate ab initio prediction. J. Nucl. Mater. 494, 172–181. https://doi.org/10.1016/j.jnucmat.2017.07.026

Johnson, J.W., Oelkers, E.H., Helgeson, H.C., 1992. SUPCRT92: A software package for calculating the standard molal thermodynamic properties of minerals, gases, aqueous species, and reactions from 1 to 5000 bar and 0 to 1000°C. Comput. Geosci. 18, 899–947. https://doi.org/10.1016/0098-3004(92)90029-Q

Jonasson, R., Bancroft, G., Nesbitt, H., 1985. Solubilities of some hydrous REE phosphates with implications for diagenesis and sea water concentrations. Geochim. Cosmochim. Acta 49, 2133–2139. https://doi.org/10.1016/0016-7037(85)90071-7

de Kerdaniel, E.D.F., Clavier, N., Dacheux, N., Terra, O., Podor, R., 2007. Actinide solubility-controlling phases during the dissolution of phosphate ceramics. J. Nucl. Mater. 362, 451–458. https://doi.org/10.1016/j.jnucmat.2007.01.132

Kestin, J., Sengers, J.V., Kamgar-parsi, B., Sengers, J.M.H.L., 1984. Thermophysical Properties of Fluid D_2O. J. Phys. Chem. Ref. Data 13, 601–609. https://doi.org/10.1063/1.555714

Kielland, J., 1937. Individual Activity Coefficients of Ions in Aqueous Solutions. J. Am. Chem. Soc. 59, 1675–1678. https://pubs.acs.org/doi/pdf/10.1021/ja01288a032

Kinniburgh, D., Cooper, D., 2011. PhreePlot: Creating graphical output with PHREEQC. 574.

Kulik, D.A., Wagner, T., Dmytrieva, S.V., Kosakowski, G., Hingerl, F.F., Chudnenko, K.V., Berner, U.R., 2013. GEM-Selektor geochemical modeling package: Revised algorithm and GEMS3K numerical kernel for coupled simulation codes. Comput. Geosci. 17, 1–24. https://doi.org/10.1007/s10596-012-9310-6

Liu, X., Byrne, R.H., 1997. Rare earth and yttrium phosphate solubilities in aqueous solution. Geochim. Cosmochim. Acta 61, 1625–1633. https://doi.org/10.1016/S0016-7037(97)00037-9

Louvel, M., Etschmann, B., Guan, Q., Testemale, D., Brugger, J., 2022. Carbonate complexation enhances hydrothermal transport of rare earth elements in alkaline fluids. Nat. Commun. 13, 1456. https://doi.org/10.1038/s41467-022-28943-z

Mesbah, A., Clavier, N., Elkaim, E., Szenknect, S., Dacheux, N., 2017. In pursuit of the rhabdophane crystal structure: from the hydrated monoclinic $LnPO_4 \cdot 0.667H_2O$ to the hexagonal $LnPO_4$ (Ln = Nd, Sm, Gd, Eu and Dy). J. Solid State Chem. 249, 221–227. https://doi.org/10.1016/j.jssc.2017.03.004

Michard, A., 1989. Rare earth element systematics in hydrothermal fluids. Geochim. Cosmochim. Acta 53, 745–750. https://doi.org/10.1016/0016-7037(89)90017-3

Migdisov, A.A., Williams-Jones, A.E., 2007. An experimental study of the solubility and speciation of neodymium (III) fluoride in F-bearing aqueous solutions. Geochim. Cosmochim. Acta 71, 3056–3069. https://doi.org/10.1016/j.gca.2007.04.004

Migdisov, A.A., Williams-Jones, A.E., Wagner, T., 2009. An experimental study of the solubility and speciation of the Rare Earth Elements (III) in fluoride- and chloride-bearing aqueous solutions at temperatures up to 300 °C. Geochim. Cosmochim. Acta 73, 7087–7109. https://doi.org/10.1016/j.gca.2009.08.023

Migdisov, A.A., Williams-Jones, A.E., 2014. Hydrothermal transport and deposition of the rare earth elements by fluorine-bearing aqueous liquids. Miner. Depos. 49, 987–997. https://doi.org/10.1007/s00126-014-0554-z

Migdisov, A.A., Williams-Jones, A.E., Brugger, J., Caporuscio, F.A., 2016. Hydrothermal transport, deposition, and fractionation of the REE: Experimental data and thermodynamic calculations. Chem. Geol. 439, 13–42. https://doi.org/10.1016/j.chemgeo.2016.06.005

Miron, G.D., Kulik, D.A., Dmytrieva, S.V., Wagner, T., 2015. GEMSFITS: Code package for optimization of geochemical model parameters and inverse modeling. J. Appl. Geochem. 55, 28–45. https://doi.org/10.1016/j.apgeochem.2014.10.013

Miron, G.D., Wagner, T., Kulik, D.A., Heinrich, C.A., 2016. Internally consistent thermodynamic data for aqueous species in the system Na-K-Al-Si-O-H-Cl. Geochim. Cosmochim. Acta 187, 41–78. https://doi.org/10.1016/j.gca.2016.04.026

Miron, G.D., Wagner, T., Kulik, D.A., Lothenbach, B., 2017. An internally consistent thermodynamic dataset for aqueous species in the system Ca-Mg-Na-K-Al-Si-O-H-C-Cl to 800 °C and 5 kbar. Am. J. Sci. 317, 755–806. https://doi.org/10.2475/07.2017.01

Navrotsky, A., Lee, W., Mielewczyk-Gryn, A., Ushakov, S.V., Anderko, A., Wu, H., Riman, R.E., 2015. Thermodynamics of solid phases containing rare earth oxides. The Journal of Chemical Thermodynamics 88, 126–141. https://doi.org/10.1016/j.jct.2015.04.008

Ni, Y., Hughes, J. M., and Mariano, A. N., 1995. Crystal chemistry of the monazite and xenotime structures. Am. Mineral. 80, 21–26. https://doi.org/10.2138/am-1995-1-203

Nisbet, H., Migdisov, A.A., Williams-Jones, A.E., van Hinsberg, V.J., Xu, H., Roback, R., 2022. The solubility of thorium in carbonate-bearing solutions at hydrothermal conditions. Geochim. Cosmochim. Acta 330, 80–92. https://doi.org/10.1016/j.gca.2021.04.035

Perry, E.P., Gysi, A.P., 2018. Rare earth elements in mineral deposits: Speciation in hydrothermal fluids and partitioning in calcite. Geofluids 2018, 21–26. https://doi.org/10.1155/2018/5382480

Poitrasson, F., Oelkers, E., Schott, J., Montel, J.M., 2004. Experimental determination of synthetic $NdPO_4$ monazite end-member solubility in water from 21°C to 300°C: Implications for rare earth element mobility in crustal fluids. Geochim. Cosmochim. Acta 68, 2207–2221. https://doi.org/10.1016/j.gca.2003.12.010

Popa, K., Konings, R.J.M., 2006. High-temperature heat capacities of $EuPO_4$ and $SmPO_4$ synthetic monazites. Thermochim. Acta 445, 49–52. https://doi.org/10.1016/j.tca.2006.03.023

Popa, K., Jutier, F., Wastin, F., Konings, R.J.M., 2006a. The heat capacity of $NdPO_4$. J. Chem. Thermodyn. 38, 1306–1311. https://doi.org/10.1016/j.jct.2006.02.006

Popa, K., Sedmidubský, D., Beneš, O., Thiriet, C., Konings, R.J.M., 2006b. The high-temperature heat capacity of $LnPO_4$ (Ln = La, Ce, Gd) by drop calorimetry. J. Chem. Thermodyn. 38, 825–829. https://doi.org/10.1016/j.jct.2005.08.019

Pourtier, E., Devidal, J.L., Gibert, F., 2010. Solubility measurements of synthetic neodymium monazite as a function of temperature at 2 kbars, and aqueous neodymium speciation in equilibrium with monazite. Geochim. Cosmochim. Acta 74, 1872–1891. https://doi.org/10.1016/j.gca.2009.12.023

Powell, M.J., 2009. The BOBYQA algorithm for bound constrained optimization without derivatives. Cambridge NA Report NA2009/06, University of Cambridge, Cambridge 26.

Rafiuddin, M.R., Mueller, E., Grosvenor, A. P., 2014. X-ray spectroscopic study of the electronic structure of monazite- and xenotime-type rare-earth phosphates. J. Phys. Chem. C 118, 18000–18009. https://doi.org/10.1021/jp5051996

Rai, D., Felmy, A.R., Yui, M., 2003. Thermodynamic model for the solubility of $NdPO_4$(c) in the aqueous Na^+-H^+-$H_2PO_4^-$- HPO_4^{2-}-OH^--Cl^--H_2O system. J. Radioanal. Nucl. Chem. 256, 37–43. https://doi.org/10.1023/A:1023339723535

Richter, L., Diamond, L.W., Atanasova, P., Banks, D.A., Gutzmer, J., 2018. Hydrothermal formation of heavy rare earth element (HREE)-xenotime deposits at 100 °C in a sedimentary basin. Geology 46, 263–266. https://doi.org/10.1130/G39871.1

Robinson, R.A., Stokes, R.H., 1968. Electrolyte Solutions, 2nd Edition, London.

Roncal-Herrero, T., Rodríguez-Blanco, J.D., Oelkers, E.H., Benning, L.G., 2011. The direct precipitation of rhabdophane ($REEPO_4 \cdot H_2O$) nano-rods from acidic aqueous solutions at 5-100 °C. J. Nanoparticle Res. 13, 4049–4062. https://doi.org/10.1007/s11051-011-0347-6

Schijf, J., Byrne, R.H., 2021. Speciation of yttrium and the rare earth elements in seawater: Review of a 20-year analytical journey. Chem. Geol. 584, 120479. https://doi.org/10.1016/j.chemgeo.2021.120479

Shannon, R.D., 1976. Revised effective ionic radii and systematic studies of interatomic distances in halides and chalcogenides. Acta crystallographica section A: crystal physics, diffraction, theoretical and general crystallography 32(5), 751–767. https://doi.org/10.1107/S0567739476001551

Shelyug, A., Mesbah, A., Szenknect, S., Clavier, N., Dacheux, N., Navrotsky, A., 2018. Thermodynamics and stability of rhabdophanes, hydrated rare earth phosphates $REPO_4 \cdot n H_2O$. Front. Chem. 6, 1–11. https://doi.org/10.3389/fchem.2018.00604

Shock, E.L., Helgeson, H.C., 1988. Calculation of the thermodynamic and transport properties of aqueous species at high pressures and temperatures: Correlation algorithms for ionic species and equation of state predictions to 5 kb and 1000°C. Geochim. Cosmochim. Acta 52, 2009–2036. https://doi.org/10.1016/0016-7037(88)90181-0

Shock, E.L., Helgeson, H.C., Sverjensky, D.A., 1989. Calculation of the thermodynamic and transport properties of aqueous species at high pressures and temperatures: Standard partial molal properties of inorganic neutral species. Geochim. Cosmochim. Acta 53, 2157–2183. https://doi.org/10.1016/0016-7037(89)90341-4

Shock, E.L., Oelkers, E.H., Johnson, J.W., Sverjensky, D.A., Helgeson, H.C., 1992. Calculation of the thermodynamic properties of aqueous species at high pressures and temperatures. Effective electrostatic radii, dissociation constants and standard partial molal properties to 1000°C and 5 kbar. J. Chem. Soc., Faraday Trans. 88, 803–826. https://doi.org/10.1039/FT9928800803

Shock, E.L., Sassani, D.C., Willis, M., Sverjensky, D.A., 1997. Inorganic species in geologic fluids: Correlations among standard molal thermodynamic properties of aqueous ions and hydroxide complexes. Geochim. Cosmochim. Acta 61, 907–950. https://doi.org/10.1016/S0016-7037(96)00339-0

Smith, M.P., Henderson, P., Zhang, P., 1999. Reaction relationships in the Bayan Obo Fe-REE-Nb deposit Inner Mongolia, China: implications for the relative stability of rare-earth element phosphates and fluorocarbonates. Contrib. to Mineral. Petrol. 134, 294–310. https://doi.org/10.1007/s004100050485

Smith, M.P., Moore, K., Kavecsánszki, D., Finch, A.A., Kynicky, J., Wall, F., 2016. From mantle to critical zone: A review of large and giant sized deposits of the rare earth elements. Geosci. Front. 7, 315–334. https://doi.org/10.1016/j.gsf.2015.12.006

Sverjensky, D.A., Shock, E.L., Helgeson, H.C., 1997. Prediction of the thermodynamic properties of aqueous metal complexes to 1000°C and 5 kb. Geochim. Cosmochim. Acta 61, 1359–1412. https://doi.org/10.1016/S0016-7037(97)00009-4

Tagirov, B.R., Zotov, A.V., Akinfiev, N.N., 1997. Experimental study of dissociation of HCl from 350 to 500°C and from 500 to 2500 bars: Thermodynamic properties of HCl°(aq). Geochim. Cosmochim. Acta 61, 4267–4280. https://doi.org/10.1016/S0016-7037(97)00274-3

Tananaev, I., Vasil'eva, V.P., 1963, Lanthanum phosphates. Russ. J. Inorg. Chem., 555–558.

Tanger, J.C., Helgeson, H.C., 1988. Calculation of the thermodynamic and transport properties of aqueous species at high pressures and temperatures; revised equations of state for the standard partial molal properties of ions and electrolytes. Am. J. Sci. 288, 19–98. https://doi.org/10.2475/ajs.288.1.19

Thiriet, C., Konings, R. J. M., Javorský, P., Magnani, N., Wastin, F., (2005). The low temperature heat capacity of $LaPO_4$ and $GdPO_4$, the thermodynamic functions of the monazite-type $LnPO_4$ series. J. Chem. Thermodyn. 37, 131–139. https://doi.org/10.1016/j.jct.2004.07.031

Thiriet, C., Konings, R.J.M., Javorský, P., Wastin, F., 2004. The heat capacity of cerium orthophosphate $CePO_4$, the synthetic analogue of monazite. Phys. Chem. Miner. 31, 347–352. https://doi.org/10.1007/s00269-004-0397-8

Tiedeman, C.R., Hill, M.C., 2007. Model calibration and issues related to validation, sensitivity analysis, post-audit, uncertainty evaluation and assessment of prediction data needs. Groundwater: Resource Evaluation, Augmentation, Contamination, Restoration, Modeling and Management, 237–282.

Tyurin, A.V., Ryumin, M.A., Khoroshilov, A.V., Gurevich, V.M., Gavrichev, K.S., 2020. Thermodynamic functions of holmium orthophosphate $HoPO_4$ in the range 9–1370 K. Thermochim. Acta 683. https://doi.org/10.1016/j.tca.2019.178459

Ushakov, S.V., Helean K.B., Navrotsky, A., Boatner, L.A., 2001. Thermochemistry of rare-earth orthophosphates. J. Mater. Res. 16, 2623–2633. https://doi.org/10.1557/JMR.2001.0361

Van Hoozen, C.J., Gysi, A.P., Harlov, D.E., 2020. The solubility of monazite ($LaPO_4$, $PrPO_4$, $NdPO_4$, and $EuPO_4$) endmembers in aqueous solutions from 100 to 250 °C. Geochim. Cosmochim. Acta 280, 302–316. https://doi.org/10.1016/j.gca.2020.04.019

Verplanck, P.L., 2017. The Role of Fluids in the Formation of Rare Earth Element Deposits. Procedia Earth Planet. Sci. 17, 758–761. https://doi.org/10.1016/j.proeps.2017.01.014

Verplanck, P.L., Lang Farmer, G., Kettler, R.M., Lowers, H.A., Johnson, C.A., Koenig, A.E., Blessington, M.J., 2022. Petrogenesis and rare earth element mineralization of the Elk Creek carbonatite, Nebraska, USA. Ore Geol. Rev. 146, 104953. https://doi.org/10.1016/j.oregeorev.2022.104953

Wagner, T., Kulik, D.A., Hingerl, F.F., Dmytrievava, S.V., 2012. Gem-selektor geochemical modeling package: TSolMod library and data interface for multicomponent phase models. Can. Mineral. 50, 1173–1195. https://doi.org/10.3749/canmin.50.5.1173

Williams-Jones, A.E., Samson, I.M., Olivo, G.R., 2000. The genesis of hydrothermal fluorite-REE deposits in the Gallinas Mountains, New Mexico. Econ. Geol. 95, 327–341. https://doi.org/10.2113/gsecongeo.95.2.327

Wood, S.A., Palmer, D.A., Wesolowski, D.J., Bénézeth, P., 2002. The aqueous geochemistry of the rare earth elements and yttrium. Part XI. The solubility of $Nd(OH)_3$ and hydrolysis of Nd^{3+} from 30 to 290 °C at saturated water vapor pressure with in-situ pHm measurement. Water–rock interactions, ore deposits, and environmental geochemistry: a tribute to David Crerar, Special Publication 7, 229–256.

Zimmer, K., Zhang, Y., Lu, P., Chen, Y., Zhang, G., Dalkilic, M., Zhu, C., 2016. SUPCRTBL: A revised and extended thermodynamic dataset and software package of SUPCRT92. Comput. Geosci. 90, 97–111. https://doi.org/10.1016/j.cageo.2016.02.013

674

Figure Captions

Figure 1. Comparison of predicted [Supcrt92] and experimentally derived solubility constants ($\log K_{sp}$) as a function of $10^3/T$ (K) for LREE phosphates (monazite and rhabdophane) at 25−300 °C. Lines represent the predicted solubility constants using calorimetric data for REE phosphates (Tables 2 and 3) and aqueous species from Supcrt92 (Table S1). The symbols represent experimental $\log K_{sp}$ values reported from previous studies as summarized in Tables S3 and S4. Solubility data: B&K93: Byrne and Kim (1993); C05: Cetiner et al. (2005), F&B91: Firsching and Brune (1991); F&B91 (R): Recalculated by Byrne and Kim (1993) based on Firsching and Brune (1991); GA16: Gausse et al. (2016); GY18: Gysi et al. (2018); J85: Jonasson et al. (1985); J85 (R): Recalculated by Byrne and Kim (1993) based on Jonasson et al. (1985); L&B97: Liu and Byrne (1997); P04: Poitrasson et al. (2004); R03: Rai et al. (2003); T&V63: Recalculated by Byrne and Kim (1993) based on Tananaev and Vasil'eva (1963); VH20: Van Hoozen et al. (2020).

Figure 2. Comparison of predicted [Supcrt92] and experimentally derived solubility constants ($\log K_{sp}$) as a function of $10^3/T$ (K) for HREE phosphates (xenotime) at 25−300 °C and *swvp*. Lines represent the predicted solubility constants using calorimetric data for REE phosphates (Tables 2 and 3) and aqueous species from Supcrt92 (Table S1). The symbols represent experimental $\log K_{sp}$ values reported from previous studies as in Table S4. GY15: Gysi et al. (2015); GH21: Gysi and Harlov (2021). Other abbreviations of references can be found in Fig. 1.

Figure 3. Total **(a)** Nd and **(b)** Er concentrations (logarithm molality) and calculated molalities of aqueous REE species controlling monazite (Mnz), rhabdophane (Rab), and xenotime (Xtm) solubility between 25 and 300 °C. The plots show a comparison (before thermodynamic optimization) between experimental solubility data (ThermoExp_REE database) and predicted solubilities calculated using Supcrt92 for aqueous species (Table A1; and REE chloride from Migdisov et al., 2009) and REE phosphate thermodynamic properties from Tables 2 and 3. The reported experimental conditions are pH of 1 in HCl-based solutions for Rab and pH of 2 in $HClO_4$-based solutions for Mnz/Xtm. Solubility data: GY15 (Gysi et al., 2015); GA16 (Gausse et al., 2016); VH20 (Van Hoozen et al., 2020); [Supcrt92] includes data from Haas et al. (1995), Shock et al. (1997), and Sverjensky et al. (1997); REE chloride data from M09 (Migdisov et al., 2009).

Figure 4. Comparison between monazite and rhabdophane solubility data and the new predictions using the optimized thermodynamic data for aqueous REE species (FIT 1−3 in Tables 5 and 6), showing the logarithm of dissolved REE molality as a function of temperature between 25 and 300 °C. Also shown are the previous predictions using the Supcrt92 dataset for aqueous REE species. Solubility data: GA16 (Gausse et al., 2016); GY18 (Gysi et al., 2018); VH20 (Van Hoozen et al., 2020). Note that the experimental solubility data for rhabdophane are plotted here only for reference; due to the varying HCl concentrations from 0.1 to 0.5 mol L^{-1} in the experiments by Gausse et al. (2016) the average HCl concentrations (Table S3) are used to calculate the predicted and optimized rhabdophane solubility.

Figure 5. Comparison between xenotime solubility data and the new predictions using the optimized thermodynamic data for aqueous REE species (FIT 1−3 in Table 6) showing the logarithm of dissolved REE molality as a function of temperature between 25 and 300 °C at *swvp*. Also shown are the previous predictions using the Supcrt92 dataset for aqueous REE species. Solubility data: GY15 (Gysi et al., 2015) and VH21 (Gysi and Harlov, 2021). Here, a lower bound (~10 kJ/mol) for the $\Delta_f G^\circ_{298}$ of $HREEOH^{2+}$ in FIT 1 is defined due to that the xenotime solubilities are mainly controlled by the $HREE^{3+}$ species at the referred temperature range.

Figure 6. Logarithm molality of dissolved LREE concentrations showing a comparison between predicted versus measured concentrations controlled by rhabdophane solubility (Poitrasson et al., 2004; Cetiner et al., 2005; Gausse et al., 2016). Predictions are based on aqueous species properties from **(a)** the Supcrt92 dataset and **(b)** from the optimized $\Delta_f G^\circ_{298}$ values derived in this study (FIT 2 in Table 5). The correlations are considerably improved in (b) using the optimized aqueous species from this study; $\sigma = \sqrt{\frac{1}{N}\sum_{i=1}^{N}(M_{(p)i} - M_m)^2}$, where $M_{(p)i}$ is predicted molality and M_m is the measured molality, N is the number of samples.

Figure 7. Diagrams showing the logarithm molality of dissolved REE and aqueous speciation as a function of temperature between 25 and 300 °C at *swvp* in experimental solutions in equilibrium with **(a)** Mnz-(Nd), and **(b)** Xtm-(Er), respectively. A comparison is shown between experimental solubility data (Table S3), predictions using the aqueous REE species properties from Supcrt92 (Table S1), and predictions using the optimized $\Delta_f G^\circ_{298}$ values for aqueous REE species from Table 6 (FIT 1 for Mnz; FIT 2 for Xtm). Monazite-(Nd) experiments by Van Hoozen et al. (2020) and

xenotime-(Er) experiments by Gysi and Harlov (2021) were conducted in $HClO_4$ solution with pH of 2. Note that the lines of Er Total [FIT 2] and Er^{3+} [FIT 2] in **(b)** are overlapping.

Figure 8. Calculated vs. experimental solubility constants of LREE phosphates (monazite and rhabdophane) as a function of $10^3/T$(K) at 25−300 °C and *swvp*. The solid lines represent the predicted logK_{sp} values of monazite and rhabdophane using the fitted coefficients from Table 7 (FIT 1 for monazite and FIT 2 for rhabdophane optimized in this study); the dashed lines were calculated using the aqueous species from Supcrt92 (Table S1) and the calorimetric data for REE phosphates from Tables 2 and 3.The symbols represent re-evaluated experimental logK_{sp} values (GY18/VH20, P04, and GA06), which were calculated in GEMSFITS using the optimized $\Delta_f G^\circ_{298}$ values for aqueous REE species (Tables 5 and 6) and equilibrium speciation using as input the experimental database compiled in this study (ThermoExp_REE in the supplementary data). Other literature logK_{sp} values (B&K93, J85, J85(R), F&B91, R03, L&B97, F&B91(R), and T&v63) are shown for comparison. Reference abbreviations are the same as in Fig. 1.

Figure 9. Calculated vs. experimental solubility constants of HREE phosphates (xenotime) as a function of $10^3/T$(K) at 25−300 °C and *swvp*. Solid lines represent the predicted logK_{sp} values of xenotime (≥ 100 °C) using the fitted coefficients from Table 7 (FIT 2 for xenotime optimized in this study); the dashed lines were calculated using the aqueous species from Supcrt92 (Table S1) and the calorimetric data for REE phosphates from Table 2. The symbols represent experimental logK_{sp} values (GY15/GH21) which were calculated in GEMSFITS using the optimized $\Delta_f G^\circ_{298}$ values for aqueous REE species (Table 6) and equilibrium speciation using as input the experimental database compiled in this study (ThermoExp_REE in the supplementary data). Other literature logK_{sp} values (F&B91, L&B97, F&B91(R), B&K93, J85, and J85(R)) are shown for comparison. Reference abbreviations are the same as in Fig. 2.

Figure 10. Predicted (dashed lines) and experimental (symbols) logK_{sp} values between 100 and 300 °C. The predictions are calculated using the fitted coefficients from Table 7. The experimental data were re-calculated in GEMSFITS using the optimized $\Delta_f G^\circ_{298}$ values for aqueous REE species (Table 6) and equilibrium speciation using as input the experimental database compiled in this study (ThermoExp_REE in the supplementary data). Reference abbreviations are the same as Fig. 1.

Figure 11. Comparison of experimental and optimized REE phosphate logK_{sp} values determined at 298.15 K and 1 bar. REE^{3+} ionic radii data are from Shannon (1976) based on 9 coordination number for monazite and rhabdophane, and 8 coordination number for xenotime. Abbreviations of references are same as Fig. 1.

Figure 12. Logarithm of total dissolved REE molality versus temperature from 25 to 300 °C showing the predicted monazite and xenotime endmember solubilities in acidic perchlorate solution (pH of 2). Predictions were calculated using GEM-Selektor and the thermodynamic properties for aqueous REE species from **(a)** Supcrt92 (Table S1) and **(b)** optimized in this study (Table 6). The thermodynamic properties of other aqueous species are from Table S1 and minerals are from Tables 2 and 3. The non-optimized solubility data, bold lines in (a), indicate that Nd^{3+} and Er^{3+} control monazite-(Nd) and xenotime-(Er) solubility at T<280 °C, respectively, and $NdOH^{2+}$ and $ErOH^{2+}$at >280 °C. The optimized solubility data, bold lines in (b), indicate that Nd^{3+} controls monazite-(Nd) solubility at T<100 °C, and $NdOH^{2+}$ at >150 °C; Er^{3+} controls xenotime-(Er) solubility from 25 to 300 °C.

Figure 13. Logarithm molality of Nd and Er aqueous species in equilibrium with **(a)** monazite and **(b)** xenotime as a function of pH (2–9) calculated using a titration model and GEM-Selektor at 250 °C and *swvp.* The pH of the fluids were varied by adding an acid ($HClO_4$ concentrations of 1.25×10^{-2}m to 1.0×10^{-9}m) or by adding a base (NaOH concentrations of 1.0×10^{-9}m to 1.15×10^{-2}m). The figures show a comparison between the calculated speciation using Supcrt92 (Table S1) for aqueous species vs. the optimized thermodynamic data from Table 6. Speciation calculations for other LREE and HREE can be found in Figs. S3 and S4, respectively.

Table 1. List of aqueous species and data sources used in the speciation calculation. The thermodynamic properties of REE aqueous species are listed in the supplementary data (Table S1).

		Species	References
REE Species	Major species:	REE^{3+}	1, 2
		$REEOH^{2+}$	4
		$REECl^{2+}$	5
	Minor species:	$REE(OH)_2^{+}$, $REE(OH)_4^{-}$, $REE(OH)_3^{0}$, $REECl_3^{0}$	4
		$REECl_2^{+}$	5
P Species	Major species:	$H_3PO_4^{0}$,	3
		$H_2PO_4^{-}$, HPO_4^{2-}, PO_4^{3-}	1, 2
	Minor species:	$H_2P_2O_7^{2-}$, $H_3P_2O_7^{-}$, $H_4P_2O_7^{0}$, $HP_2O_7^{3-}$, $P_2O_7^{4-}$	1, 2
Other Species		ClO_4^{-}, Cl^{-}, OH^{-}, H^{+}	1, 2
		HCl^{0}	6
		Na^{+}, $NaOH^{0}$, $NaCl^{0}$	7

References: [1]Shock et al. (1997); [2]Shock and Helgeson (1988); [3]Shock et al. (1989); [4]Haas et al. (1995); [5]Migdisov et al. (2009); [6]Tagirov et al. (1997); [7]Miron et al. (2016)

Table 2. Standard thermodynamic properties of monazite and xenotime (at reference temperature of 298.15 K and pressure of 1 bar) and heat capacity function ($Cp^\circ = a + bT + c/T^2 + d/T^{0.5} + eT^2$, with T in Kelvin) derived from calorimetric measurements unless otherwise noted. A full compilation is listed in the supplementary data (Table S2).

REEPO$_4$	$\Delta_f G^\circ_{298}$	$\Delta_f H^\circ_{298}$	S°_{298}	V°_m	Cp°_{298}	$Cp^\circ = a + bT + c/T^2 + d/T^{0.5} + eT^2$					T range
	kJ mol^{-1}	kJ mol^{-1}	J mol^{-1}K^{-1}	J bar^{-1}	J mol^{-1}K^{-1}	a	b	c	d	e	K
LaPO$_4$	-1850.5[1]	-1970.7 ± 1.8[2]	108.24[3]	4.603[4]	101.28[5]	121.128	3.01 × 10^{-2}	-2.56 × 10^6	-	-	450–1570[5]
CePO$_4$	-1847.5[6]	-1967.8 ± 2.4[2]	119.97[1, 3]	4.516[4]	106.43[3, 5]	125.209	2.79 × 10^{-2}	-2.41 × 10^6	-	-	450–1570[5]
PrPO$_4$	-1850.5[1]	-1969.5 ± 3.7[2]	123.24[1]	4.445[4]	106.04[7]	124.500	3.04 × 10^{-2}	-2.45 × 10^6	-	-	450–1570[7]
NdPO$_4$	-1849.6[1]	-1968.4 ± 2.3[2]	125.53[1]	4.386[4]	104.80[8]	132.963	2.25 × 10^{-2}	-3.10 × 10^6	-	-	300–1570[8]
SmPO$_4$	-1846.9[1, 6]	-1965.7 ± 2.4[2]	122.49[1]	4.281[4]	105.60[7]	133.125	2.35 × 10^{-2}	-3.07 × 10^6	-	-	450–1570[7]
EuPO$_4$	-1747.8 ± 2.8[9]	-1870.6 ± 2.6[2]	117.21[1]	4.240[4]	111.50[7]	137.560	1.77 × 10^{-2}	-2.79 × 10^6	-	-	450–1570[7]
GdPO$_4$	-1844.5[6]	-1962.2 ± 4.4[2]	124.57[1]	4.201[4]	102.21[5]	133.237	1.28 × 10^{-2}	-3.10 × 10^6	-	-	450–1570[5]
YPO$_4$	-1867.9 ± 1.7[10]	-1987.7 ± 1.7[2]	93.86 ± 0.08[10]	4.314[4]	99.27 ± 0.02[10]	161.000	4.21 × 10^{-3}	-2.66 × 10^6	-594.30	3.92 × 10^{-6}	298–1600[11]
TbPO$_4$	-1851.4	-1971.1 ± 4.6[2]	123.10[12]	4.390[4]	105.30[13]	116.400	4.55 × 10^{-2}	-2.19 × 10^6	-	-	298–1373[14]
DyPO$_4$	-1829.1[11]	-1967.9 ± 2.6[2]	119.00[11]	4.335[4]	105.27	185.500	0.00	-3.26 × 10^6	-751.90		300–900[15]
HoPO$_4$	-1851.6 ± 3.4[16]	-1971.6 ± 3.4[2]	123.80[12]	4.290[4]	102.70 ± 0.10[16]	124.400	2.66 × 10^{-2}	-2.69 × 10^6	-	-	298–1373[14]
ErPO$_4$	-1855.4 ± 2.1[17]	-1976.9 ± 2.1[2]	116.63 ± 0.06[17]	4.237[4]	101.08 ± 0.06[17]	207.200	0.00	-5.29 × 10^5	-1661.0		300–900[15]
TmPO$_4$	-1844.0	-1964.7 ± 4.7[2]	120.50[12]	4.200[4]	99.70[14]	128.800	1.90 × 10^{-2}	-3.09 × 10^6	-	-	298–1373[14]
YbPO$_4$	-1809.8 ± 4.9[18]	-1929.4 ± 4.9[2, 18]	109.70 ± 0.10[18]	4.164[4]	102.20 ± 0.10[18]	247.600	-2.29 × 10^{-2}	2.56 × 10^5	-2463.0	6.87 × 10^{-6}	298–1800[11]
LuPO$_4$	-1835.4 ± 4.2[19]	-1955.4 ± 4.2[2]	99.74 ± 0.32[19]	4.122[4]	100.00 ± 0.10[19]	130.700	1.85 × 10^{-2}	-3.33 × 10^6	-	-	298–1373[14]

References: [1]Thiriet et al. (2005), hybrid adiabatic relaxation calorimetry & differential scanning calorimetry; [2]Ushakov et al. (2001), oxide-melt calorimetry; [3]Thiriet et al. (2004), hybrid adiabatic relaxation calorimetry & differential scanning calorimetry; [4]Ni et al. (1995), X-ray diffraction; [5]Popa et al. (2006a), drop calorimetry; [6]Gysi et al. (2018), solubility experiments; [7]Popa and Konings (2006), drop calorimetry; [8]Popa et al. (2006b), hybrid adiabatic relaxation calorimetry & drop calorimetry; [9]Gavrichev et al. (2009), adiabatic calorimetry; [10]Gavrichev et al. (2010), adiabatic calorimetry; [11]Gysi et al. (2015), solubility experiments; [12]Ji et al. (2017), derived from ab initio; [13]Gavrichev et al. (2013a), adiabatic calorimetry; [14]Gysi and Harlov (2021), solubility experiments; [15]Gysi et al. (2016), differential scanning calorimetry; [16]Tyurin et al. (2020), adiabatic calorimetry & differential scanning calorimetry; [17]Gavrichev et al. (2012), adiabatic & drop calorimetry; [18]Gavrichev et al. (2013b), adiabatic & drop calorimetry; [19]Gavrichev et al. (2006), adiabatic calorimetry.

Table 3. Standard thermodynamic properties selected for rhabdophane ($REEPO_4 \cdot nH_2O$) at reference temperature of 298.15 K and pressure of 1 bar and solubility product ($\log K_{sp} = a0 + a2/T^2$, with T in Kelvin) derived by Gausse et al. (2016).

[1]$REEPO_4 \cdot nH_2O$	[2]$\Delta_r G^\circ_{298}$ kJ mol^{-1}	[3]$\Delta_r H^\circ_{298}$ kJ mol^{-1}	[3]$\Delta_r S^\circ_{298}$ J mol^{-1}K^{-1}	[1]V°_m J/bar	[4]$\log K_{sp}$	[5]$\log K_{sp} = a0 + a2/T^2$		T range °C
						a0	a2	
$LaPO_4 \cdot 0.804H_2O$	141.56	-26 ± 11	-562.0	5.705	-24.8 ± 0.6	-29.355	1358.1	25–90
$CePO_4 \cdot 0.732H_2O$	144.41	-21 ± 7	-554.8	5.610	-25.3 ± 0.8	-28.979	1096.9	25–90
$PrPO_4 \cdot 0.709H_2O$	146.13	-30 ± 8	-590.7	5.568	-25.6 ± 0.8	-30.856	1567.0	25–90
$NdPO_4 \cdot 0.746H_2O$	144.98	-22 ± 4	-560.1	5.437	-25.4 ± 0.6	-29.254	1149.1	25–90
$SmPO_4 \cdot 0.636H_2O$	143.84	-22 ± 8	-556.2	5.347	-25.2 ± 1.3	-29.054	1149.1	25–90
$EuPO_4 \cdot 0.555H_2O$	142.13	-17 ± 7	-533.7	5.270	-24.9 ± 1.7	-27.878	887.97	25–90
$GdPO_4 \cdot 0.533H_2O$	142.70	-25 ± 10	-562.5	5.220	-25.0 ± 0.3	-29.380	1305.8	25–90

[1]Unit-cell parameters (H_2O content and V°_m) of rhabdophane are experimentally measured by Shelyug et al. (2018);
[2]$\Delta_r G^\circ_{298}$ values are calculated by the solubility products (Gausse et al., 2016) based on the reaction Eq. 1;
[3]$\Delta_r H^\circ_{298}$ and $\Delta_r S^\circ_{298}$ values are from the van't Hoff plots of the solubility results;
[4]$\log K_{sp}$ values are from the solubility experiments in Gausse et al. (2016).
[5]$\log K_{sp}$ (T) at 20–100 °C are calculated by the 2-term extrapolation; This extrapolation assumes that $\Delta_r Cp^\circ$ is a constant (0) for the Eq. 1.

Table 4. Summary of monazite, xenotime, and rhabdophane solubility experiments selected for the thermodynamic data optimization and for generating the ThermoExp_REE experimental database file in the supplementary data. Electronic tables of the all the experimental data can be found in the supplementary data (Table S3).

REE	[8]Solid phases	Aqueous solutions	Experimental points (n)	[9]Direction of equilibrium	Temperature range (°C)	Pressure range (bar)	pH range	[10]Powder/ Crystal
La	[1]$LaPO_4$	H_2O-$HClO_4$-H_3PO_4	16	U	100–250	*swvp*	2	Crystal
	[3]$LaPO_4 \cdot 0.804H_2O$	H_2O-HCl/$LaCl_3$-H_3PO_4	5	U+O	25–90	1	0.78–1.15	Powder
Ce	[4]$CePO_4$	H_2O-$HClO_4$-H_3PO_4	7	U	100–250	*swvp*	2	Crystal
	[3]$CePO_4 \cdot 0.732H_2O$	H_2O-HCl/$CeCl_3$-H_3PO_4	6	U+O	25–90	1	0.64–1.07	Powder
Pr	[1]$PrPO_4$	H_2O-$HClO_4$-H_3PO_4	11	U	100–250	*swvp*	2	Crystal
	[3]$PrPO_4 \cdot 0.709H_2O$	H_2O-HCl/$PrCl_3$-H_3PO_4	6	U+O	25–90	1	0.55–1.08	Powder
Nd	[1]$NdPO_4$	H_2O-$HClO_4$-H_3PO_4	12	U	100–250	*swvp*	2	Crystal
	[5]$NdPO_4$	H_2O-HCl	2	U	200–300	*swvp*	2	Powder
	[3]$NdPO_4 \cdot 0.746H_2O$	H_2O-HCl/$NdCl_3$-H_3PO_4	6	U+O	25–90	1	0.56–1.07	Powder
Sm	[4]$SmPO_4$	H_2O-$HClO_4$-H_3PO_4	5	U	100–250	*swvp*	2	Crystal
	[2]$SmPO_4 \cdot 0.636H_2O$	H_2O+NaCl+HCl	7	U	23–50	*swvp*	1	Powder
	[2]$SmPO_4 \cdot 0.636H_2O$	H_2O+$NaClO_4$+$HClO_4$	6	U	23–50	*swvp*	1–2	Powder
	[3]$SmPO_4 \cdot 0.636H_2O$	H_2O-HCl/$SmCl_3$-H_3PO_4	6	U+O	25–90	1	0.59–1.14	Powder
Eu	[1]$EuPO_4$	H_2O-$HClO_4$-H_3PO_4	7	U	100–250	*swvp*	2	Crystal
	[3]$EuPO_4 \cdot 0.555H_2O$	H_2O-HCl/$EuCl_3$-H_3PO_4	6	U+O	25–90	1	0.68–1.14	Powder
Gd	[4]$GdPO_4$	H_2O-$HClO_4$-H_3PO_4	8	U	100–250	*swvp*	2	Crystal
	[5]$GdPO_4 \cdot 0.533H_2O$	H_2O-HCl	1	U	21	*swvp*	2	Powder
	[3]$GdPO_4 \cdot 0.533H_2O$	H_2O-HCl/$GdCl_3$-H_3PO_4	5	U+O	25–90	1	0.81–1.07	Powder
Y	[6]YPO_4	H_2O-$HClO_4$-H_3PO_4	12	U	100–250	*swvp*	2	Crystal
Tb	[7]$TbPO_4$	H_2O-$HClO_4$-H_3PO_4	14	U	100–250	*swvp*	2	Crystal
Dy	[6]$DyPO_4$	H_2O-$HClO_4$-H_3PO_4	9	U	100–250	*swvp*	2	Crystal

Ho	[7]$HoPO_4$	H_2O-$HClO_4$-H_3PO_4	13	U	100–250	*swvp*	2	Crystal
Er	[6]$ErPO_4$	H_2O-$HClO_4$-H_3PO_4	9	U	100–250	*swvp*	2	Crystal
Tm	[7]$TmPO_4$	H_2O-$HClO_4$-H_3PO_4	16	U	100–250	*swvp*	2	Crystal
Yb	[6]$YbPO_4$	H_2O-$HClO_4$-H_3PO_4	12	U	100–250	*swvp*	2	Crystal
Lu	[7]$LuPO_4$	H_2O-$HClO_4$-H_3PO_4	13	U	100–250	*swvp*	2	Crystal

[1]Van Hoozen et al. (2020); [2]Cetiner et al. (2005); [3]Gausse et al. (2016); [4]Gysi et al. (2018); [5]Poitrasson et al. (2004); [6]Gysi et al. (2015); [7]Gysi and Harlov (2021).

[8]All REE mineral phases in this column have been crystal structure identified in the literature

[9]U: equilibrium was approached from under-saturation direction; O: equilibrium was approached from over-saturation direction.

[10]Synthetic monazite or xenotime powder or mm-sized crystals

Table 5. Initial and optimized values of the standard partial molal Gibbs energy ($\Delta_f G^\circ_{298}$) of REE aqueous species using the rhabdophane solubility data at T <100 °C and optimization FIT 2 trial, from the Supcrt92 dataset (Johnson et al., 1992; Haas et al., 1995; Shock et al., 1997; Sverjensky et al., 1997) using GEMSFITS code package (Miron et al., 2015).

LREE	Species	Supcrt92	FIT 2				
		$\Delta_f G^\circ_{298}$ (J mol^{-1})	$\Delta_f G^\circ_{298}$ (J mol^{-1})	[1]diff. (kJ mol^{-1})	σ	CSS	Opt
La	La^{3+}	-686176	**-684580**	1.60	245	114	O
	$LaOH^{2+}$	-874038	-872442	1.60	245	-	C
	LaO^{+}	-819646	-818050	1.60	245	-	C
	LaO_2^{-}	-927593	-925997	1.60	245	-	C
	LaO_2H^0	-1001231	-999635	1.60	245	-	C
Ce	Ce^{3+}	-676134	**-674113**	2.02	385	116	O
	$CeOH^{2+}$	-865251	-863230	2.02	385	-	C
	CeO^{+}	-819646	-817625	2.02	385	-	C
	CeO_2^{-}	-929266	-927245	2.02	385	-	C
	CeO_2H^0	-1001231	-999210	2.02	385	-	C
Pr	Pr^{3+}	-680318	**-679236**	1.08	543	128	O
	$PrOH^{2+}$	-870272	-869190	1.08	543	-	C
	PrO^{+}	-818809	-817727	1.08	543	-	C
	PrO_2^{-}	-940145	-939063	1.08	543	-	C
	PrO_2H^0	-1002905	-1001823	1.08	543	-	C
Nd	Nd^{3+}	-671950	**-670107**	1.84	524	121	O
	$NdOH^{2+}$	-862741	-860898	1.84	524	-	C
	NdO^{+}	-811696	-809853	1.84	524	-	C
	NdO_2^{-}	-934706	-932863	1.84	524	-	C
	NdO_2H^0	-995792	-993949	1.84	524	-	C
Sm	Sm^{3+}	-665674	**-664116**	1.56	801	701	O
	$SmOH^{2+}$	-857302	-855744	1.56	801	-	C
	SmO^{+}	-808767	-807209	1.56	801	-	C
	SmO_2^{-}	-940145	-938587	1.56	801	-	C
	SmO_2H^0	-992026	-990468	1.56	801	-	C
Eu	Eu^{3+}	-574463	**-568059**	6.40	2261	52	O
	$EuOH^{2+}$	-766509	-760105	6.40	2261	-	C
	EuO^{+}	-725455	-719051	6.40	2261	-	C
	EuO_2^{-}	-842198	-835794	6.40	2261	-	C
	EuO_2H^0	-913549	-907144	6.41	2261	-	C
Gd	Gd^{3+}	-663582	**-662067**	1.52	876	121	O
	$GdOH^{2+}$	-855628	-854113	1.52	876	-	C
	GdO^{+}	-807512	-805997	1.52	876	-	C
	GdO_2^{-}	-941400	-939885	1.52	876	-	C
	GdO_2H^0	-993700	-992185	1.52	876	-	C

[1]diff. = $\Delta_f G^\circ_{298}$ (FIT) − $\Delta_f G^\circ_{298}$ (Supcrt92)

Note that the standard deviation (σ) in the optimization was calculated by the Monte Carlo simulations. The values in bold are the optimized $\Delta_f G^\circ_{298}$ of REE aqueous species at <100 °C

Abbreviations: Opt: Optimization; O: Optimized; F: Fixed; C: Constrained

Table 6. Initial and optimized values of the standard partial molal Gibbs energy ($\Delta_f G^\circ_{298}$) of REE aqueous species using the monazite and xenotime solubility data at $T \geq 100$ °C and the three optimization fits (FIT 1–3).

REE	Species	Supcrt92	FIT 1					FIT 2					FIT 3				
		$\Delta_f G^\circ_{298}$ (J mol^{-1})	$\Delta_f G^\circ_{298}$ (J mol^{-1})	diff. (kJ mol^{-1})	σ	CSS	Opt	$\Delta_f G^\circ_{298}$ (J mol^{-1})	diff. (kJ mol^{-1})	σ	CSS	Opt	$\Delta_f G^\circ_{298}$ (J mol^{-1})	diff. (kJ mol^{-1})	σ	CSS	Opt
La	La^{3+}	-686176	**-683281**	2.90	507	127	O	-685380	0.80	882	187	O	-	-	-	-	F
	$LaOH^{2+}$	-874038	**-888550**	-14.51	1127	85	O	-	-	-	-	F	-886625	-12.59	4122	56	O
	LaO^+	-819646	-816751	2.90	507	-	C	-818850	0.80	882	-	C	-832233	-12.59	4122	-	C
	LaO_2^-	-927593	-924698	2.90	507	-	C	-926797	0.80	882	-	C	-940180	-12.59	4122	-	C
	LaO_2H^0	-1001231	-998336	2.90	507	-	C	-1000435	0.80	882	-	C	-1013818	-12.59	4122	-	C
Ce	Ce^{3+}	-676134	**-674723**	1.41	395	65	O	-678331	-2.20	1612	119	O	-	-	-	-	F
	$CeOH^{2+}$	-865251	**-881654**	-16.40	543	76	O	-	-	-	-	F	-881045	-15.79	797	66	O
	CeO^+	-819646	-818235	1.41	395	-	C	-821843	-2.20	1612	-	C	-835440	-15.79	797	-	C
	CeO_2^-	-929266	-927855	1.41	395	-	C	-931463	-2.20	1612	-	C	-945060	-15.79	797	-	C
	CeO_2H^0	-1001231	-999820	1.41	395	-	C	-1003428	-2.20	1612	-	C	-1017025	-15.79	797	-	C
Pr	Pr^{3+}	-680318	**-682140**	-1.82	593	84	O	-685620	-5.30	449	159	O	-	-	-	-	F
	$PrOH^{2+}$	-870272	**-891585**	-21.31	663	100	O	-	-	-	-	F	-892515	-22.24	815	100	O
	PrO^+	-818809	-820631	-1.82	593	-	C	-824110	-5.30	449	-	C	-841052	-22.24	815	-	C
	PrO_2^-	-940145	-941967	-1.82	593	-	C	-945447	-5.30	449	-	C	-962388	-22.24	815	-	C
	PrO_2H^0	-1002905	-1004727	-1.82	593	-	C	-1008207	-5.30	449	-	C	-1025148	-22.24	815	-	C
Nd	Nd^{3+}	-671950	**-681771**	-9.82	1026	95	O	-684633	-12.68	1193	166	O	-	-	-	-	F
	$NdOH^{2+}$	-862741	**-887916**	-25.18	1521	100	O	-	-	-	-	F	-892515	-29.77	1226	211	O
	NdO^+	-811696	-821517	-9.82	1026	-	C	-824379	-12.68	1193	-	C	-841470	-29.77	1226	-	C
	NdO_2^-	-934706	-944527	-9.82	1026	-	C	-947389	-12.68	1193	-	C	-964480	-29.77	1226	-	C
	NdO_2H^0	-995792	-1005613	-9.82	1026	-	C	-1008475	-12.68	1193	-	C	-1025566	-29.77	1226	-	C
Sm	Sm^{3+}	-665674	**-669326**	-3.65	12324	9	O	-676000	-10.33	273	104	O	-	-	-	-	F
	$SmOH^{2+}$	-857302	**-888444**	-31.14	1039	126	O	-	-	-	-	F	-888670	-31.37	950	133	O
	SmO^+	-808767	-812419	-3.65	12324	-	C	-819093	-10.33	273	-	C	-840135	-31.37	950	-	C
	SmO_2^-	-940145	-943797	-3.65	12324	-	C	-950471	-10.33	273	-	C	-971513	-31.37	950	-	C
	SmO_2H^0	-992026	-995678	-3.65	12324	-	C	-1002352	-10.33	273	-	C	-1023394	-31.37	950	-	C

Table 6. Continued

REE	Species	Supcrt92	FIT 1					FIT 2					FIT 3				
		$\Delta_f G^\circ_{298}$ (J mol^{-1})	$\Delta_f G^\circ_{298}$ (J mol^{-1})	diff. (kJ mol^{-1})	σ	CSS	Opt	$\Delta_f G^\circ_{298}$ (J mol^{-1})	diff. (kJ mol^{-1})	σ	CSS	Opt	$\Delta_f G^\circ_{298}$ (J mol^{-1})	diff. (kJ mol^{-1})	σ	CSS	Opt
Eu	Eu^{3+}	-574463	**-578864**	-4.40	2829	21	O	-587766	-13.30	1538	103	O	-		-	-	F
	$EuOH^{2+}$	-766509	**-792660**	-26.15	1316	111	O	-	-	-	-	F	-793555	-27.05	1278	129	O
	EuO^{+}	-725455	-729856	-4.40	2829	-	C	-738758	-13.30	1538	-	C	-752501	-27.05	1278	-	C
	EuO_2^{-}	-842198	-846599	-4.40	2829	-	C	-855501	-13.30	1538	-	C	-869244	-27.05	1278	-	C
	EuO_2H^0	-913549	-917950	-4.40	2829	-	C	-926852	-13.30	1538	-	C	-940595	-27.05	1278	-	C
Gd	Gd^{3+}	-663582	**-672410**	-8.83	1579	44	O	-677200	-13.62	423	125	O	-	-	-	-	F
	$GdOH^{2+}$	-855628	**-884437**	-28.81	1010	113	O	-	-13.62	-	-	F	-886311	-30.68	895	165	O
	GdO^{+}	-807512	-816340	-8.83	1579	-	C	-821130	-13.62	423	-	C	-838195	-30.68	895	-	C
	GdO_2^{-}	-941400	-950228	-8.83	1579	-	C	-955018	-13.62	423	-	C	-972083	-30.68	895	-	C
	GdO_2H^0	-993700	-1002528	-8.83	1579	-	C	-1007318	-13.62	423	-	C	-1024383	-30.68	895	-	C
Y	Y^{3+}	-685339	-706607	-21.27	537	172	O	**-706603**	-21.26	528	172	O	-	-	-	-	F
	YOH^{2+}	-878640	-879933	-1.29	12359	0.5	O	-	-	-	-	F	-918370	-39.73	1487	223	O
	YO^{+}	-828850	-850118	-21.27	537	-	C	-850114	-21.26	528	-	C	-868580	-39.73	1487	-	C
	YO_2^{-}	-951442	-972710	-21.27	537	-	C	-972706	-21.26	528	-	C	-991172	-39.73	1487	-	C
	YO_2H^0	-1011273	-1032541	-21.27	537	-	C	-1032537	-21.26	528	-	C	-1051003	-39.73	1487	-	C
Tb	Tb^{3+}	-667348	-687493	-20.15	910	171	O	**-687536**	-20.19	913	172	O	-	-	-	-	F
	$TbOH^{2+}$	-859812	-869111	-9.30	6756	2	O	-	-	-	-	F	-894277	-34.47	1425	223	O
	TbO^{+}	-812114	-832259	-20.15	910	-	C	-832302	-20.19	913	-	C	-846579	-34.47	1425	-	C
	TbO_2-	-946421	-966566	-20.15	910	-	C	-966609	-20.19	913	-	C	-980886	-34.47	1425	-	C
	TbO_2H^0	-998721	-1018866	-20.15	910	-	C	-1018909	-20.19	913	-	C	-1033186	-34.47	1425	-	C
Dy	Dy^{3+}	-664001	-686850	-22.85	479	133	O	**-686850**	-22.85	478	133	O	-	-	-	-	F
	$DyOH^{2+}$	-856465	-854057	2.41	8768	0	O	-	-	-	-	F	-898721	-42.26	1464	174	O
	DyO^{+}	-809186	-832035	-22.85	479	-	C	-832035	-22.85	478	-	C	-851442	-42.26	1464	-	C
	DyO_2^{-}	-947258	-970107	-22.85	479	-	C	-970107	-22.85	478	-	C	-989514	-42.26	1464	-	C
	DyO_2H^0	-996629	-1019478	-22.85	479	-	C	-1019478	-22.85	478	-	C	-1038885	-42.26	1464	-	C

Table 6. Continued

REE	Species	Supcrt92	FIT 1					FIT 2					FIT 3				
		$\Delta_f G^\circ_{298}$ (J mol^{-1})	$\Delta_f G^\circ_{298}$ (J mol^{-1})	diff. (kJ mol^{-1})	σ	CSS	Opt	$\Delta_f G^\circ_{298}$ (J mol^{-1})	diff. (kJ mol^{-1})	σ	CSS	Opt	$\Delta_f G^\circ_{298}$ (J mol^{-1})	diff. (kJ mol^{-1})	σ	CSS	Opt
Ho	Ho^{3+}	-675298	-682674	-7.38	120	147	O	**-682674**	-7.38	137	166	O	-	-	-	-	F
	$HoOH^{2+}$	-868180	-879521	-11.34	2410	28	O	-	-	-	-	F	-892780	-24.60	1129	188	O
	HoO^{+}	-820901	-828277	-7.38	120	-	C	-828277	-7.38	137	-	C	-845501	-24.60	1129	-	C
	HoO_2^{-}	-958554	-965930	-7.38	120	-	C	-965930	-7.38	137	-	C	-983154	-24.60	1129	-	C
	HoO_2H^0	-1009599	-1016976	-7.38	120	-	C	-1016976	-7.38	137	-	C	-1034199	-24.60	1129	-	C
Er	Er^{3+}	-669022	-695207	-26.19	373	143	O	**-695206**	-26.18	373	143	O	-	-	-	-	F
	$ErOH^{2+}$	-861904	-840715	21.19	2956	0	O	-	-	-	-	F	-903582	-41.68	1974	186	O
	ErO^{+}	-815043	-841228	-26.19	373	-	C	-841227	-26.18	373	-	C	-856721	-41.68	1974	-	C
	ErO_2^{-}	-957299	-983484	-26.19	373	-	C	-983483	-26.18	373	-	C	-998977	-41.68	1974	-	C
	ErO_2H^0	-1004578	-1030763	-26.19	373	-	C	-1030762	-26.18	373	-	C	-1046256	-41.68	1974	-	C
Tm	Tm^{3+}	-669022	-677587	-8.57	690	182	O	**-677775**	-8.75	675	187	O	-	-	-	-	F
	$TmOH^{2+}$	-862322	-868634	-6.31	4729	9	O	-	-	-	-	F	-886050	-23.73	968	202	O
	TmO^{+}	-815462	-824027	-8.57	690	-	C	-824215	-8.75	675	-	C	-839190	-23.73	968	-	C
	TmO_2^{-}	-956881	-965446	-8.57	690	-	C	-965634	-8.75	675	-	C	-980609	-23.73	968	-	C
	TmO_2H^0	-1005415	-1013980	-8.57	690	-	C	-1014168	-8.75	675	-	C	-1029143	-23.73	968	-	C
Yb	Yb^{3+}	-640152	-643023	-2.87	404	140	O	**-642974**	-2.82	399	137	O	-	-	-	-	F
	$YbOH^{2+}$	-833871	-829701	4.17	3545	2	O	-	-	-	-	F	-838377	-4.51	2629	24	O
	YbO^{+}	-787429	-790300	-2.87	404	-	C	-790251	-2.82	399	-	C	-791935	-4.51	2629	-	C
	YbO_2^{-}	-928011	-930882	-2.87	404	-	C	-930833	-2.82	399	-	C	-932517	-4.51	2629	-	C
	YbO_2H^0	-978219	-981090	-2.87	404	-	C	-981041	-2.82	399	-	C	-982725	-4.51	2629	-	C
Lu	Lu^{3+}	-666930	-665307	1.62	993	142	O	**-665536**	1.39	998	150	O	-	-	-	-	F
	$LuOH^{2+}$	-860649	-862926	-2.28	3277	28	O	-	-	-	-	F	-815126	45.52	28376	0	O
	LuO^{+}	-816717	-815094	1.62	993	-	C	-815323	1.39	998	-	C	-771194	45.52	28376	-	C
	LuO_2^{-}	-958973	-957350	1.62	993	-	C	-957579	1.39	998	-	C	-913450	45.52	28376	-	C
	LuO_2H^0	-1004997	-1003374	1.62	993	-	C	-1003603	1.39	998	-	C	-959474	45.52	28376	-	C

Note that the symbols and abbreviations in this table are the same as Table 5.
The values in bold are the optimized $\Delta_f G^\circ_{298}$ of LREE aqueous species at ≥100 °C.

Table 7. Logarithm of the solubility products (logK_{sp}) for the REE phosphates fitted as a function of temperature (T in K), and values at reference temperature of 298.15 K and pressure of 1 bar. These fits are based on the optimized thermodynamic properties for aqueous REE species from Tables 5 and 6, PO_4^{3-} and H_2O species from Table S1, and mineral properties from Tables 2 and 3. These fits and comparison to experimental data are shown in Figs. 8 and 9.

$REEPO_4$	[1]logK_{sp} = A + BT + C/T + Dlog(T) ($T \geq 100$ °C)				logK_{sp}
	A	B	C	D	298.15 K, 1 bar
$LaPO_4$	-448.41	-0.1506	1.0566×10^4	174.58	-26.00
$CePO_4$	-435.94	-0.1509	9.5878×10^4	170.35	-27.28
$PrPO_4$	-448.48	-0.1520	1.0492×10^4	174.76	-26.20
$NdPO_4$	-442.36	-0.1511	1.0212×10^4	172.48	-26.42
$SmPO_4$	-443.40	-0.1515	9.8447×10^3	172.87	-27.82
$EuPO_4$	-451.12	-0.1520	1.0661×10^4	175.57	-26.30
$GdPO_4$	-455.73	-0.1524	1.0578×10^4	177.37	-26.82
YPO_4	-499.74	-0.1570	1.2983×10^4	193.20	-24.96
$TbPO_4$	-459.23	-0.1533	1.1345×10^4	178.42	-25.41
$DyPO_4$	-466.28	-0.1542	1.1824×10^4	181.04	-24.68
$HoPO_4$	-462.98	-0.1532	1.1278×10^4	179.67	-26.28
$ErPO_4$	-462.60	-0.1535	1.1823×10^4	179.42	-24.77
$TmPO_4$	-464.25	-0.1536	1.1616×10^4	179.95	-25.83
$YbPO_4$	-461.57	-0.1537	1.1249×10^4	179.34	-25.93
$LuPO_4$	-467.43	-0.1540	1.1544×10^4	181.12	-26.46

$REEPO_4 \cdot nH_2O$	logK_{sp} = a0 + a2/T^2 (T <100 °C)		logK_{sp}
	a0	a2	298.15 K, 1 bar
$LaPO_4 \cdot 0.804H_2O$	-27.42	2.09×10^5	-25.08
$CePO_4 \cdot 0.732H_2O$	-27.48	1.62×10^5	-25.66
$PrPO_4 \cdot 0.709H_2O$	-28.57	2.48×10^5	-25.79
$NdPO_4 \cdot 0.746H_2O$	-27.66	1.72×10^5	-25.72
$SmPO_4 \cdot 0.636H_2O$	-27.44	1.75×10^5	-25.47
$EuPO_4 \cdot 0.555H_2O$	-27.04	0.90×10^5	-26.02
$GdPO_4 \cdot 0.533H_2O$	-27.52	2.01×10^5	-25.27

[1]logK_{sp} values of monazite/xenotime are calculated by $K_{sp}(Mnz/Xtm) = a(REE^{3+}) \times a(PO_4^{3-})$ based on its dissolution reaction $REEPO_4(s) = REE^{3+}(aq) + PO_4^{3-}(aq)$.

Figure 1

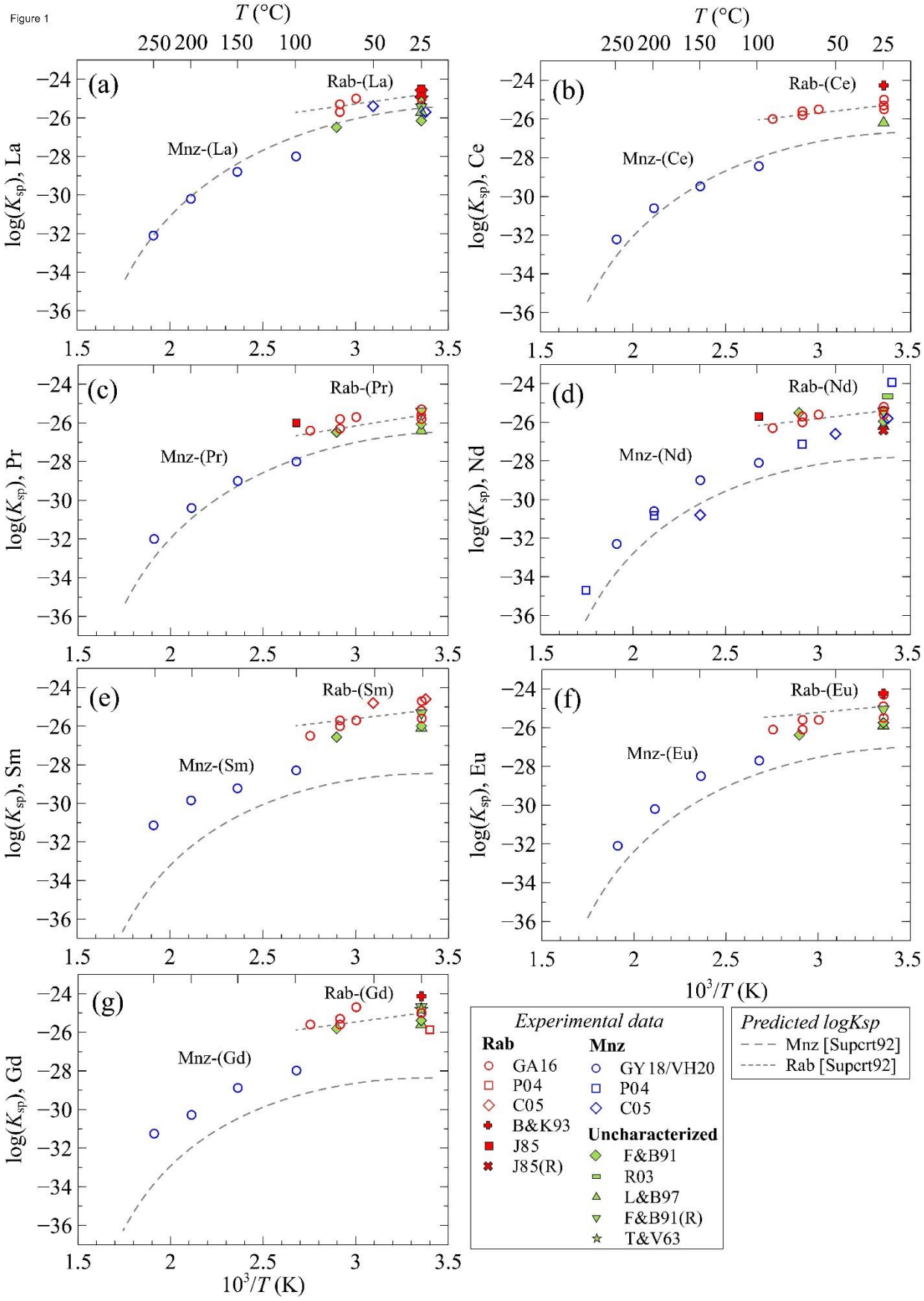
T (°C)
250 200 150 100 50 25
(a)
Rab-(La)
Mnz-(La)
log(Ksp), La
(b)
Rab-(Ce)
Mnz-(Ce)
log(Ksp), Ce
(c)
Rab-(Pr)
Mnz-(Pr)
log(Ksp), Pr
(d)
Rab-(Nd)
Mnz-(Nd)
log(Ksp), Nd
(e)
Rab-(Sm)
Mnz-(Sm)
log(Ksp), Sm
(f)
Rab-(Eu)
Mnz-(Eu)
log(Ksp), Eu
(g)
Rab-(Gd)
Mnz-(Gd)
log(Ksp), Gd
10³/T (K)
Experimental data
Rab
GA16
P04
C05
B&K93
J85
J85(R)
Mnz
GY 18/VH20
P04
C05
Uncharacterized
F&B91
R03
L&B97
F&B91(R)
T&V63
Predicted logKsp
Mnz [Supcrt92]
Rab [Supcrt92]

796

Figure 2

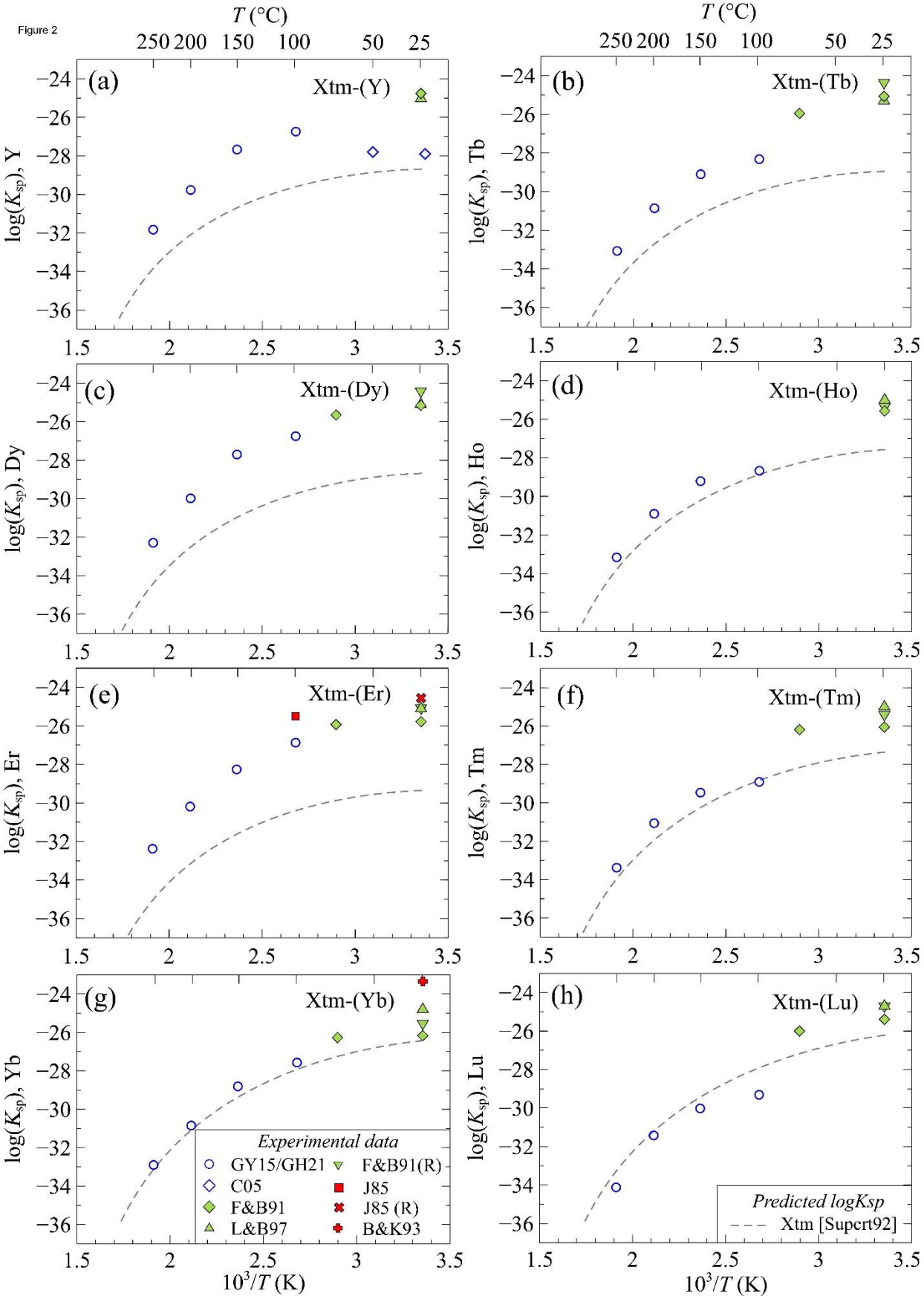
T (°C)
250 200 150 100 50 25
(a) Xtm-(Y)
(b) Xtm-(Tb)
(c) Xtm-(Dy)
(d) Xtm-(Ho)
(e) Xtm-(Er)
(f) Xtm-(Tm)
(g) Xtm-(Yb)
(h) Xtm-(Lu)
log(Ksp), Y
log(Ksp), Tb
log(Ksp), Dy
log(Ksp), Ho
log(Ksp), Er
log(Ksp), Tm
log(Ksp), Yb
log(Ksp), Lu
−24
−26
−28
−30
−32
−34
−36
1.5
2
2.5
3
3.5
10³/T (K)
Experimental data
GY15/GH21
C05
F&B91
L&B97
F&B91(R)
J85
J85 (R)
B&K93
Predicted logKsp
Xtm [Supcrt92]

797

Figure 3

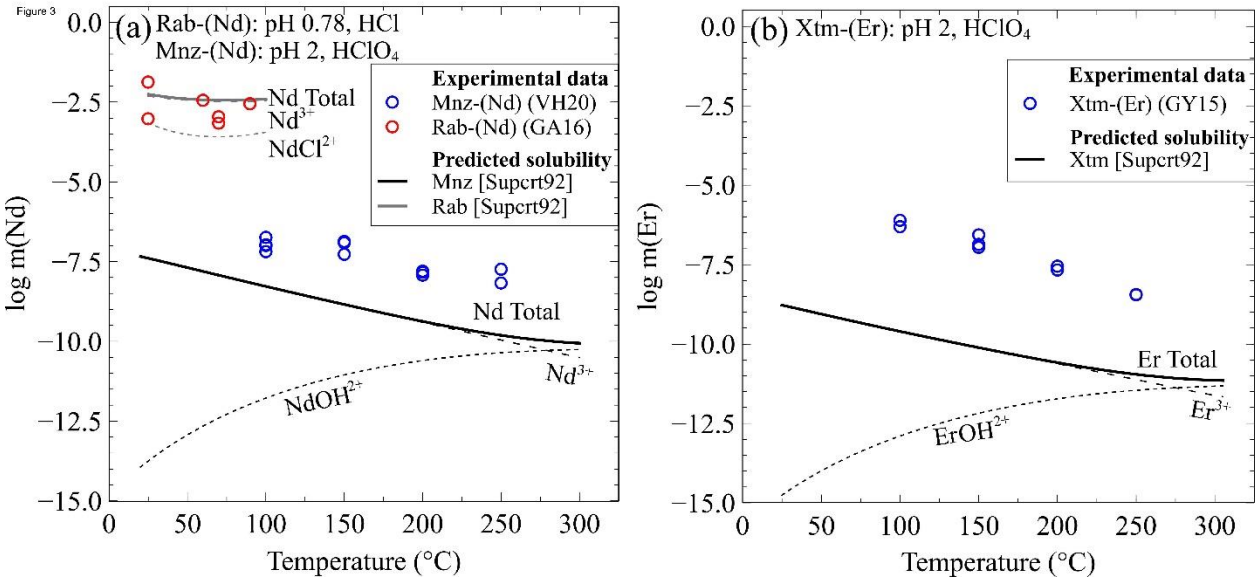

798

799

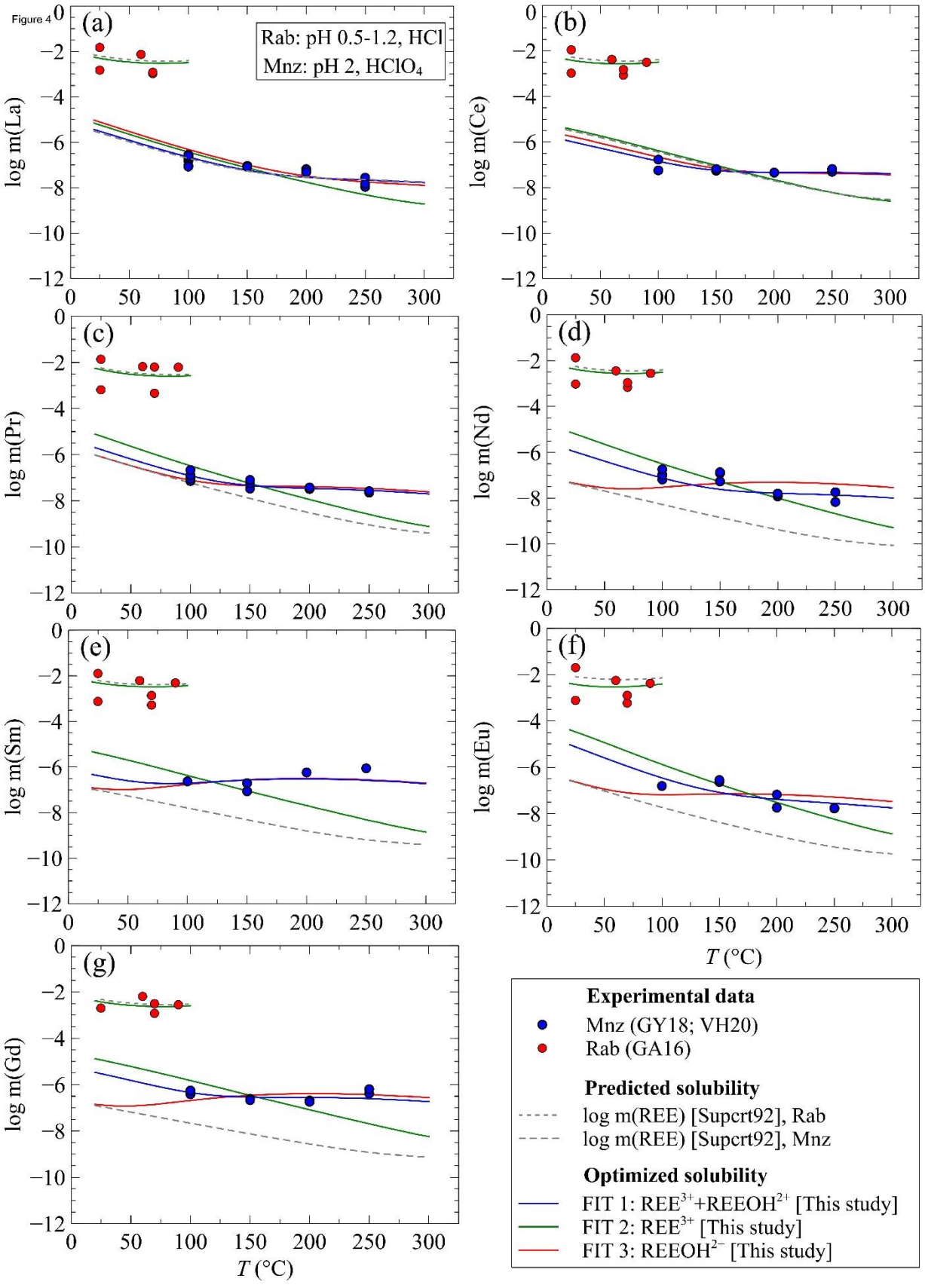
Figure 4
(a)
Rab: pH 0.5-1.2, HCl
Mnz: pH 2, HClO4
log m(La)
(b)
log m(Ce)
(c)
log m(Pr)
(d)
log m(Nd)
(e)
log m(Sm)
(f)
log m(Eu)
(g)
log m(Gd)
T (°C)
Experimental data
Mnz (GY18; VH20)
Rab (GA16)
Predicted solubility
log m(REE) [Supcrt92], Rab
log m(REE) [Supcrt92], Mnz
Optimized solubility
FIT 1: REE3+ +REEOH2+ [This study]
FIT 2: REE3+ [This study]
FIT 3: REEOH2− [This study]

800

Figure 5

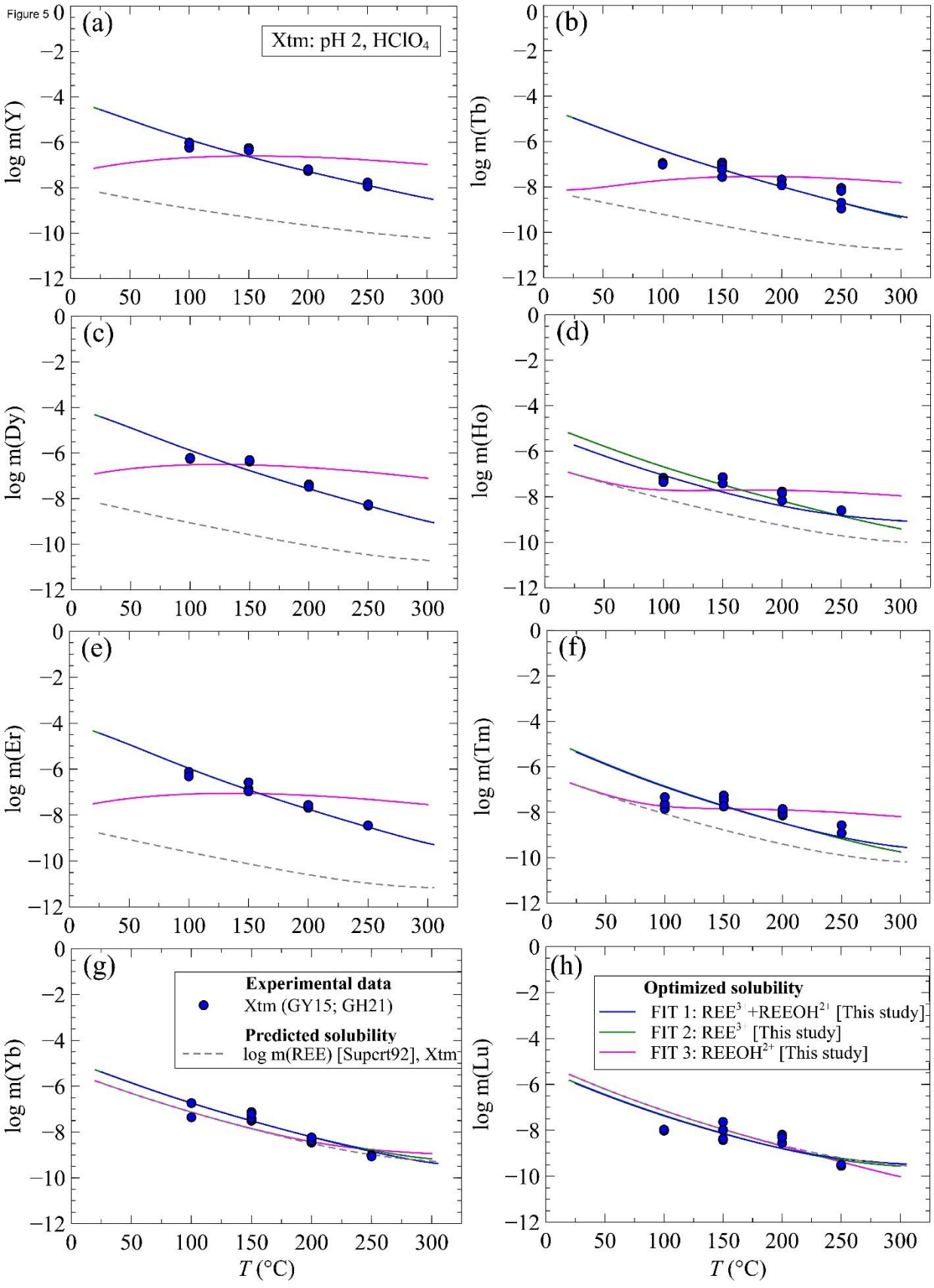
(a)
Xtm: pH 2, HClO4
log m(Y)
(b)
log m(Tb)
(c)
log m(Dy)
(d)
log m(Ho)
(e)
log m(Er)
(f)
log m(Tm)
(g)
log m(Yb)
(h)
log m(Lu)
Experimental data
Xtm (GY15; GH21)
Predicted solubility
log m(REE) [Supcrt92], Xtm
Optimized solubility
FIT 1: REE3+ +REEOH2+ [This study]
FIT 2: REE3+ [This study]
FIT 3: REEOH2+ [This study]
T (°C)
T (°C)

801

Figure 6

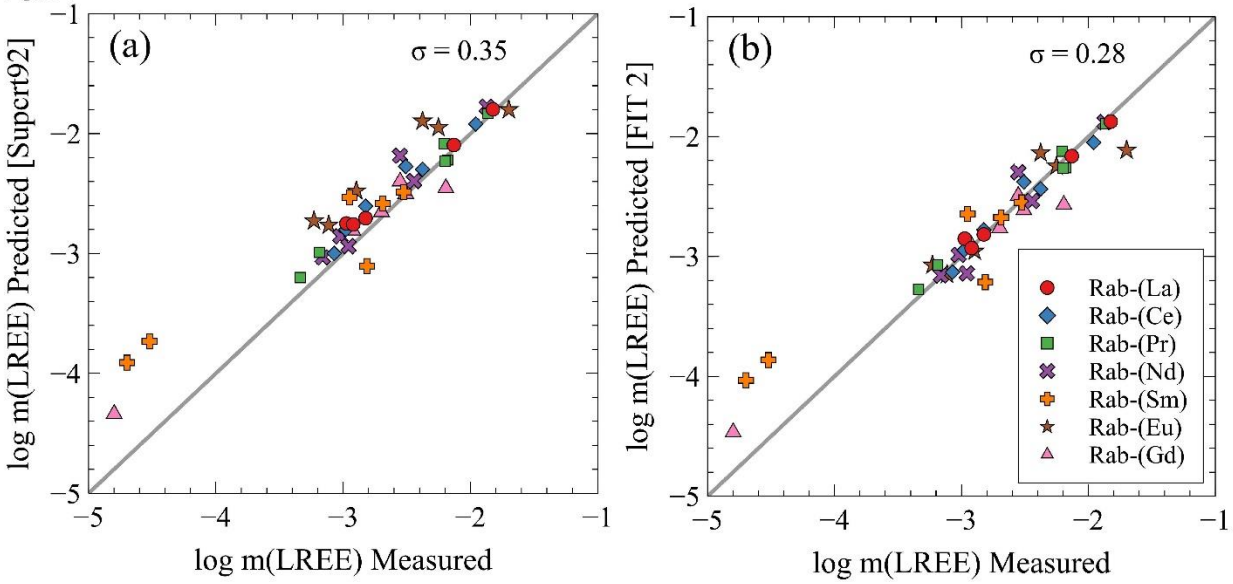
(a)
σ = 0.35
log m(LREE) Predicted [Supcrt92]
log m(LREE) Measured
(b)
σ = 0.28
log m(LREE) Predicted [FIT 2]
log m(LREE) Measured
Rab-(La)
Rab-(Ce)
Rab-(Pr)
Rab-(Nd)
Rab-(Sm)
Rab-(Eu)
Rab-(Gd)

802

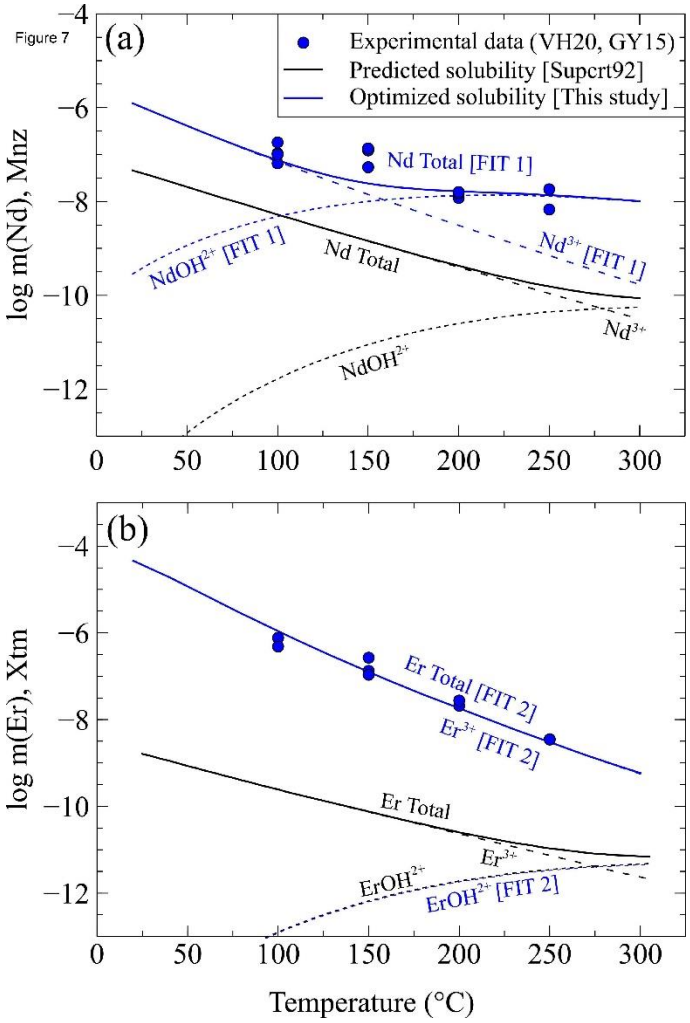
Figure 7
(a)
Experimental data (VH20, GY15)
Predicted solubility [Supcrt92]
Optimized solubility [This study]
Nd Total [FIT 1]
NdOH2+ [FIT 1]
Nd Total
Nd3+ [FIT 1]
Nd3+
NdOH2+
log m(Nd), Mnz
(b)
Er Total [FIT 2]
Er3+ [FIT 2]
Er Total
Er3+
ErOH2+
ErOH2+ [FIT 2]
log m(Er), Xtm
Temperature (°C)

803

Figure 8

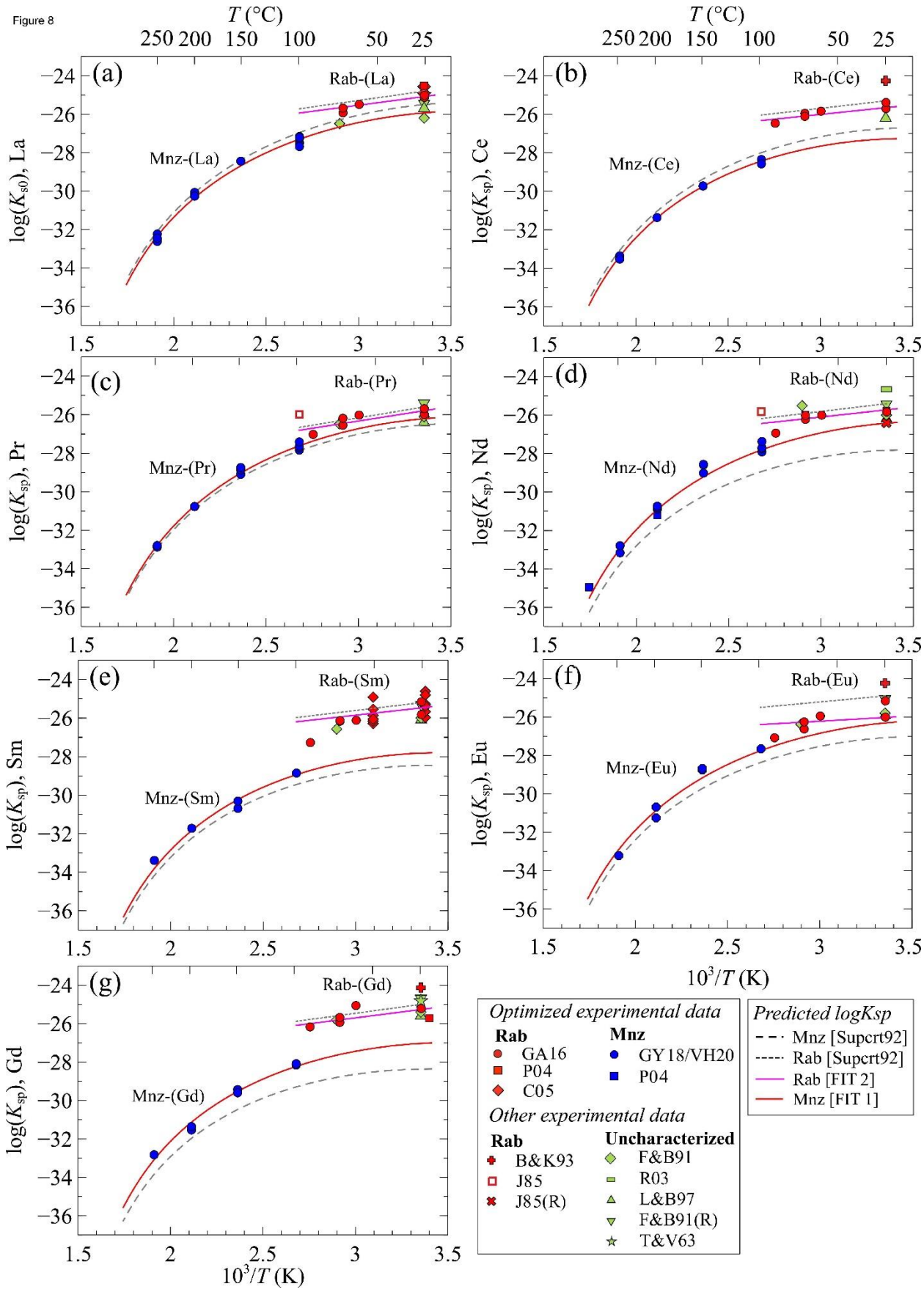
T (°C)
250 200 150 100 50 25
(a)
Rab-(La)
Mnz-(La)
log(K_s0), La
(b)
Rab-(Ce)
Mnz-(Ce)
log(K_sp), Ce
(c)
Rab-(Pr)
Mnz-(Pr)
log(K_sp), Pr
(d)
Rab-(Nd)
Mnz-(Nd)
log(K_sp), Nd
(e)
Rab-(Sm)
Mnz-(Sm)
log(K_sp), Sm
(f)
Rab-(Eu)
Mnz-(Eu)
log(K_sp), Eu
(g)
Rab-(Gd)
Mnz-(Gd)
log(K_sp), Gd
10^3/T (K)
Optimized experimental data
Rab
GA16
P04
C05
Mnz
GY18/VH20
P04
Other experimental data
Rab
B&K93
J85
J85(R)
Uncharacterized
F&B91
R03
L&B97
F&B91(R)
T&V63
Predicted logKsp
Mnz [Supcrt92]
Rab [Supcrt92]
Rab [FIT 2]
Mnz [FIT 1]

804

Figure 9

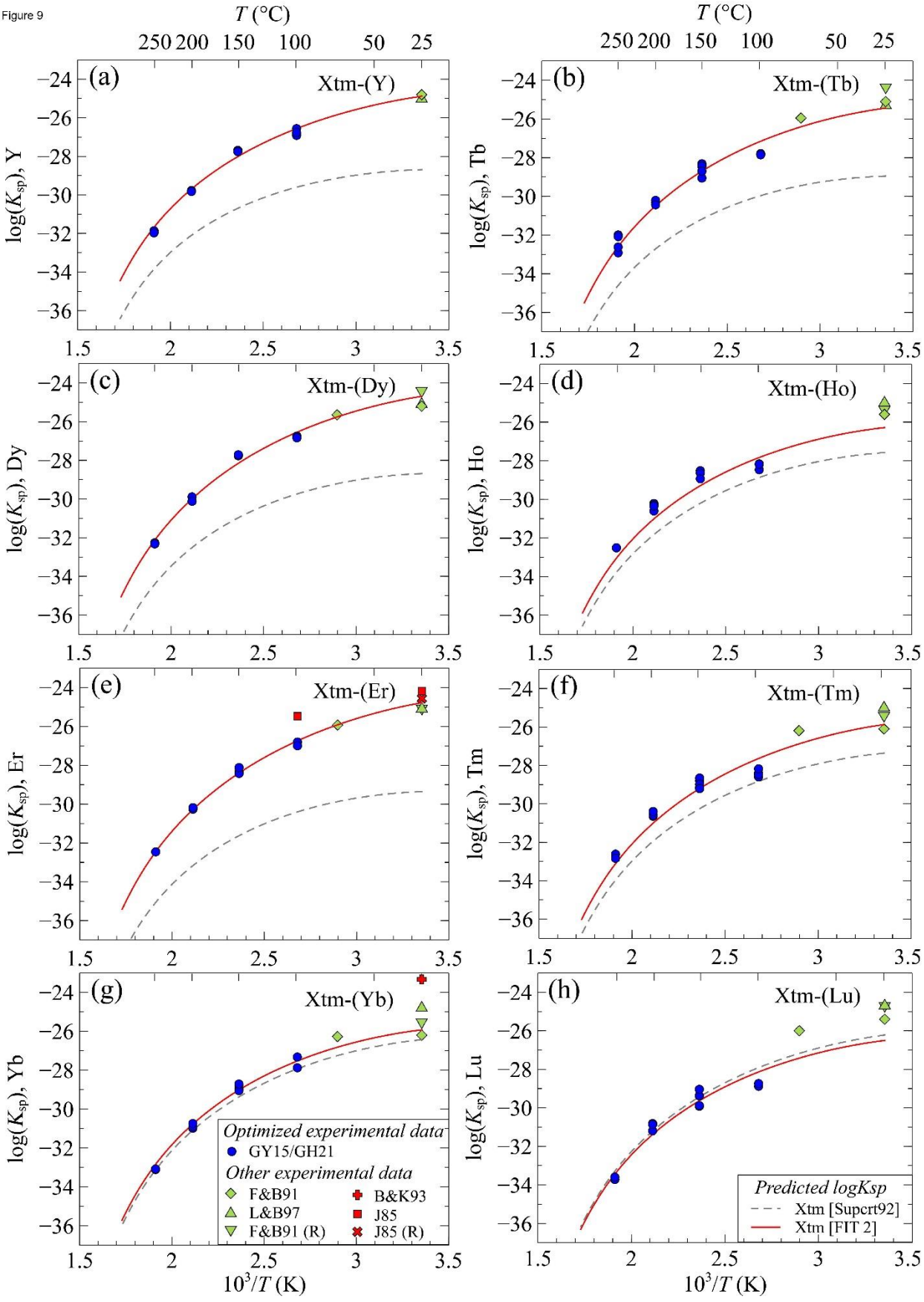
T (°C)
250 200 150 100 50 25
(a) Xtm-(Y)
(b) Xtm-(Tb)
(c) Xtm-(Dy)
(d) Xtm-(Ho)
(e) Xtm-(Er)
(f) Xtm-(Tm)
(g) Xtm-(Yb)
(h) Xtm-(Lu)
log(Ksp), Y
log(Ksp), Tb
log(Ksp), Dy
log(Ksp), Ho
log(Ksp), Er
log(Ksp), Tm
log(Ksp), Yb
log(Ksp), Lu
−24
−26
−28
−30
−32
−34
−36
1.5
2
2.5
3
3.5
10³/T (K)
Optimized experimental data
GY15/GH21
Other experimental data
F&B91
L&B97
F&B91 (R)
B&K93
J85
J85 (R)
Predicted logKsp
Xtm [Supcrt92]
Xtm [FIT 2]

805

Figure 10

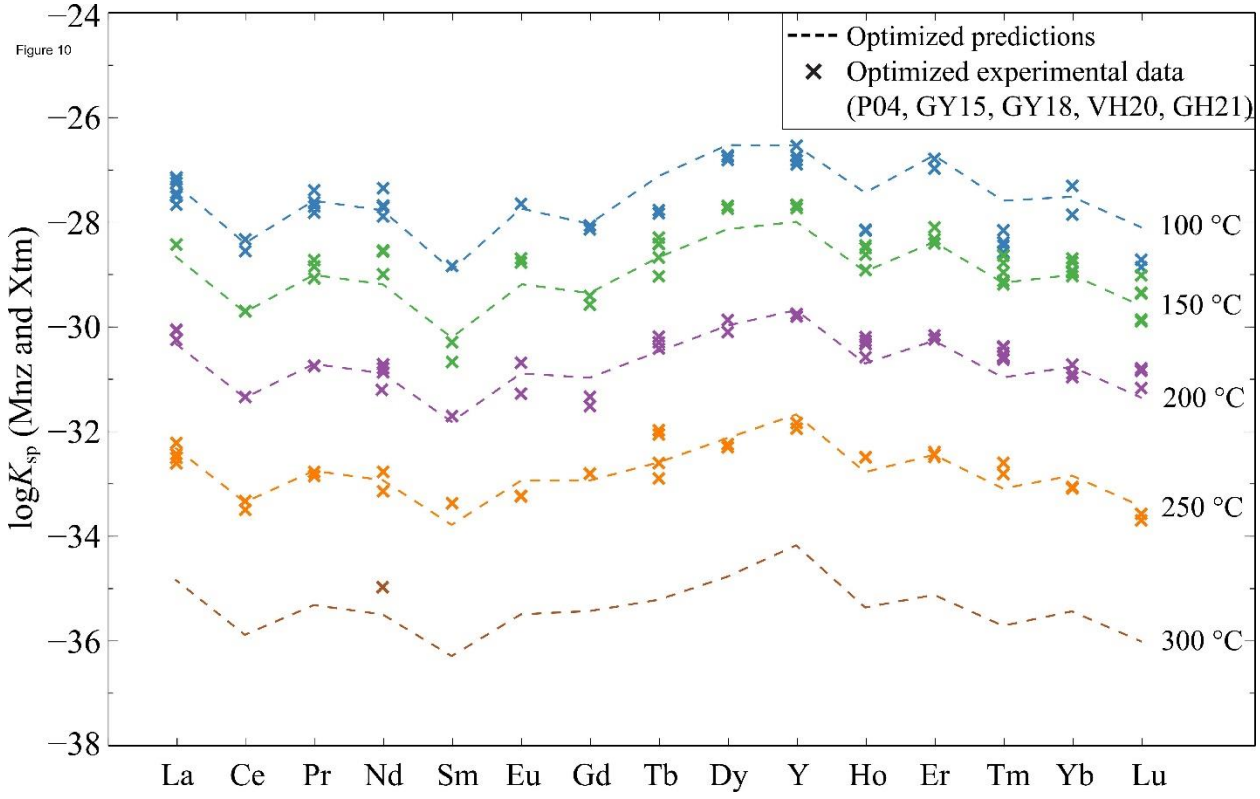

806

Figure 11

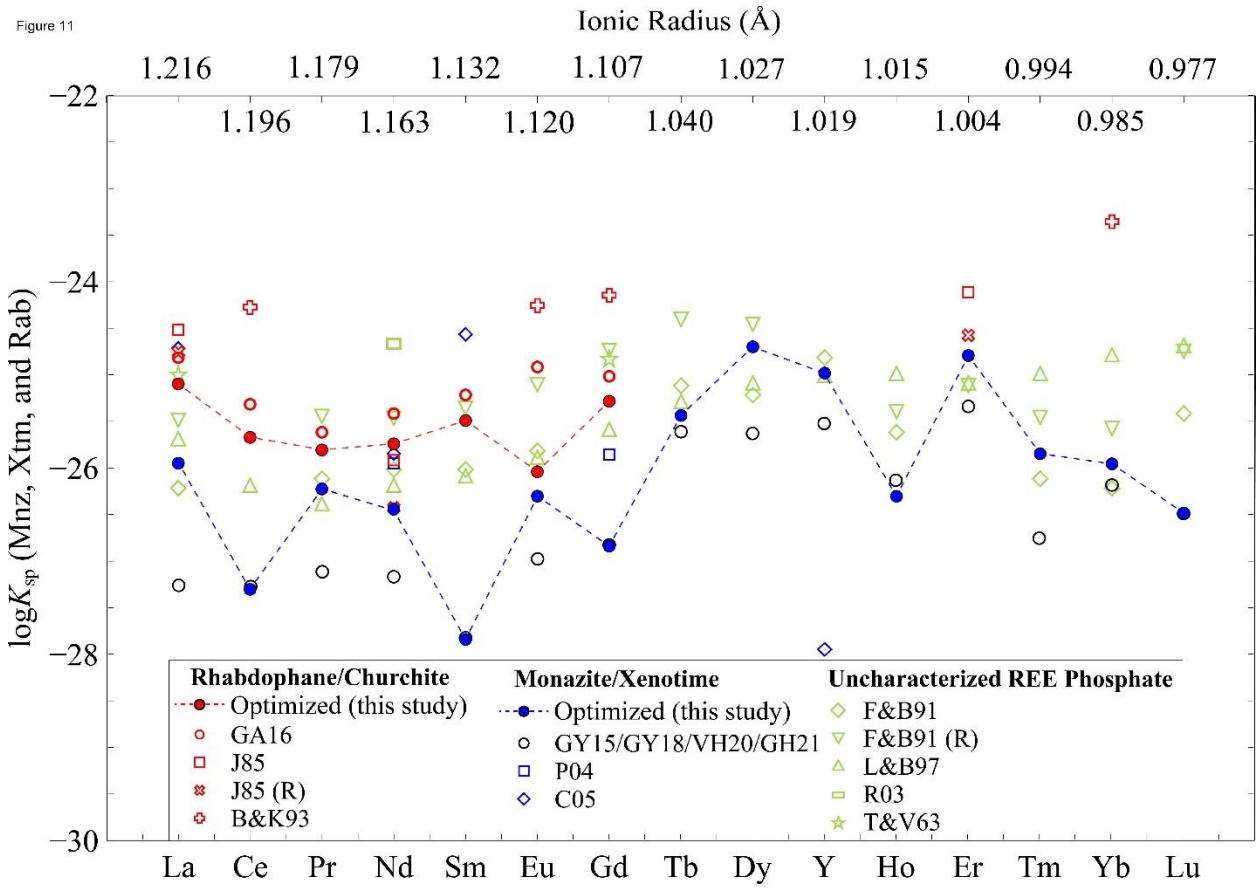

807

Figure 12

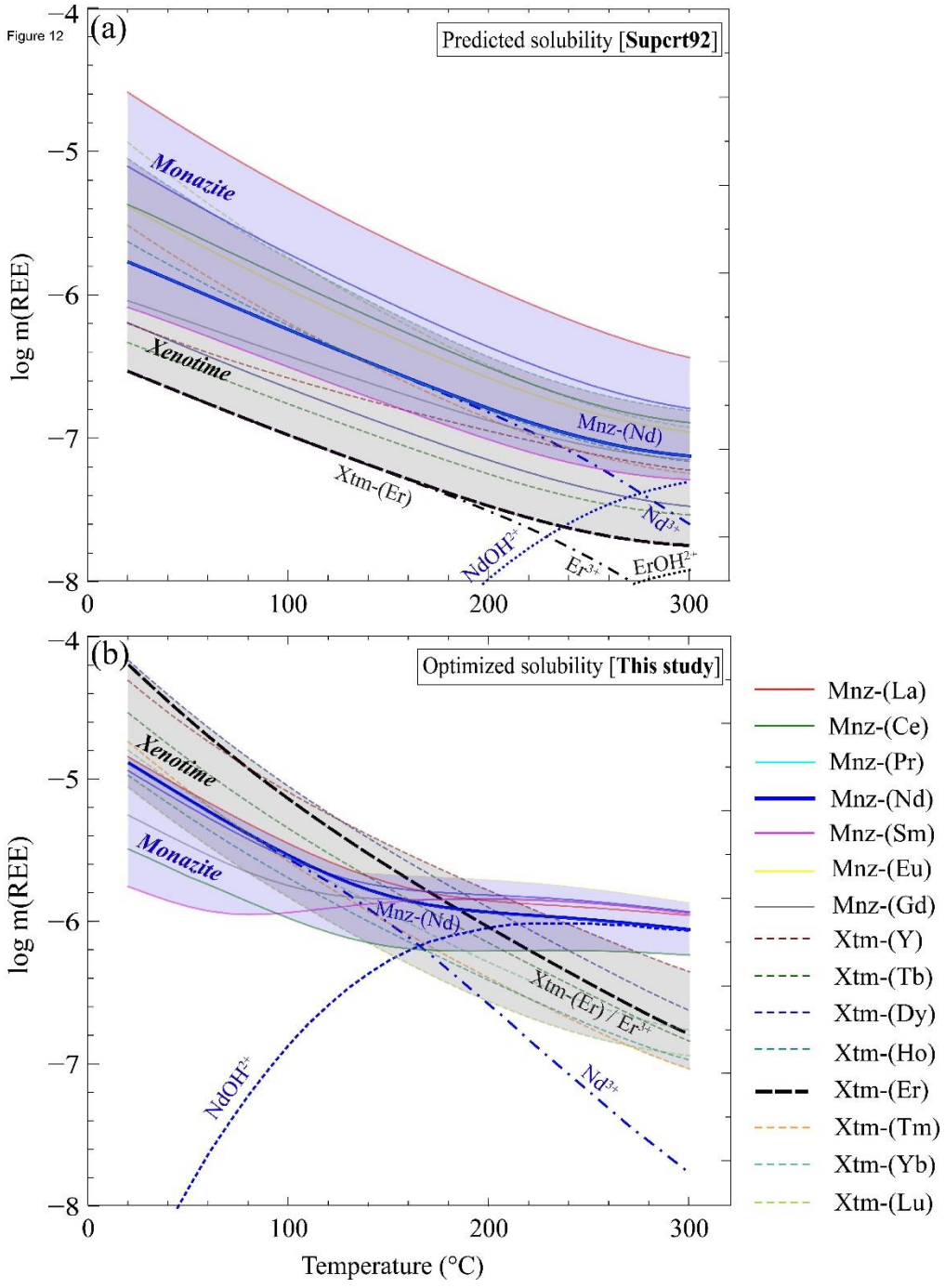

808

Figure 13

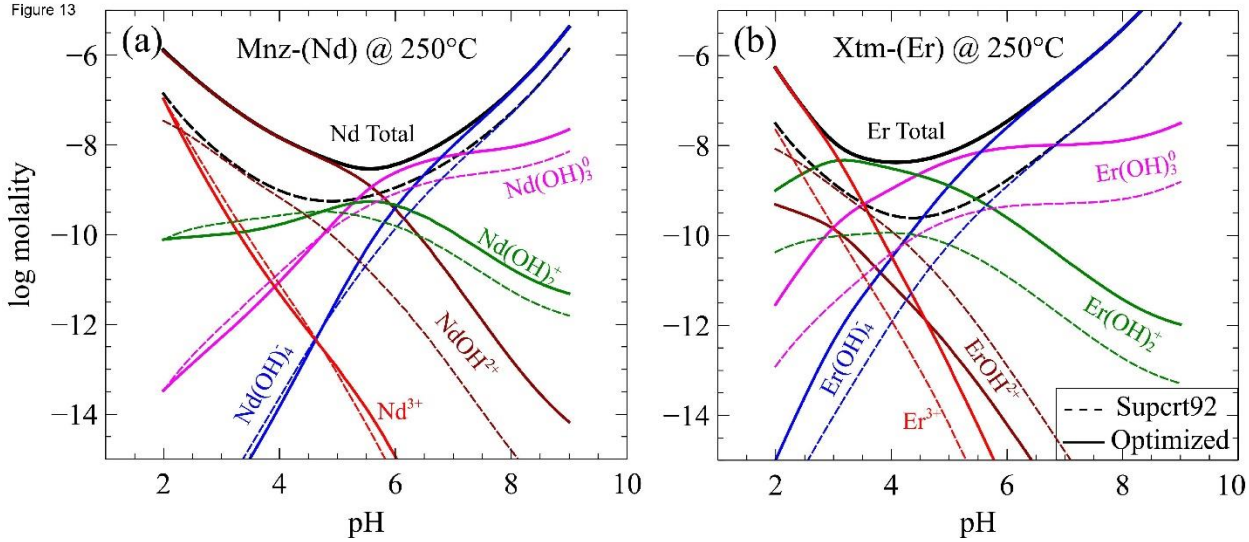

809